

We are IntechOpen, the world's leading publisher of Open Access books Built by scientists, for scientists

4,800

Open access books available

122,000

International authors and editors

135M

Downloads

Our authors are among the

154

Countries delivered to

TOP 1%

most cited scientists

12.2%

Contributors from top 500 universities



WEB OF SCIENCE™

Selection of our books indexed in the Book Citation Index
in Web of Science™ Core Collection (BKCI)

Interested in publishing with us?
Contact book.department@intechopen.com

Numbers displayed above are based on latest data collected.
For more information visit www.intechopen.com



Annealing Effects on the Metal and Semiconductor Nanowires Loaded Inside the Alumina Pores

Arūnas Jagminas
*Institute of Chemistry
Lithuania*

1. Introduction

Alumina template synthesis is a simple and cheap method for preparing arrays of nanostructural materials, such as wires, fibrils, tubes, which entails the synthesis of desired material within the cylindrically shaped pores by the respective method. To date various materials possessing anisotropic, tunneling, and giant magnetoresistance, superconductivity, semiconductivity, unusual non-linear optics, surface enhanced Raman scattering, and enhanced catalytic properties have been loaded inside the alumina pores and applied in practice. Currently the advancement of nm-scaled materials technology has prompted investigations devoted to their stability during storage in air, exploitation, irradiation, and heat-treatments under various environments. Furthermore, the heat treatment of some materials such as iron oxyhydroxides deposited inside the alumina pores seems still probably the most appropriate route to fabricate prospective magnetic nanowire arrays. The knowledge of semiconducting nanospecies thermal behavior is also crucial in their successful use to destroy selectively the tumor cells.

This paper presents our recent progress in transformation, design, characterization and potential applications of nanowired materials encased within the alumina pores upon heat treatment in air. Unexpected behavior of some metal nanowires loaded inside the alumina pores, such as iron and tin, upon heat treatment in air is presented here for the first time. As will be shown below, the heating of such arrays at proper conditions results in the formation of spinel-type FeAl_2O_4 films and SnO/SnO_2 barbed-shaped nanowire arrays. Also, the transformations of some semiconducting nanowires, particular $\text{FeO}(\text{OH})$, Cu_3Se_2 and Cu_2Se , upon heating are also presented herein. Finally, new fields of prospective applications of annealed nanowire arrays owing to gained magnetic and non-linear optical properties are discussed.

The paper is organized as follows: In the next subsection, the formation, structure and composition of most popular porous alumina templates are briefly presented. In subsection 2.2, a short overview of annealing effects, which have been reported to date for nanowire arrays loaded inside the alumina pores, is given. Our results obtained by heat treatment of nanowires of metallic iron, tin and semiconducting iron oxyhydroxide, $\text{FeO}(\text{OH})$, encapsulated within the alumina pores, are presented in section 3, while section 4 is devoted

Source: Electrodeposited Nanowires and Their Applications, Book edited by: Nicoleta Lupu,
ISBN 978-953-7619-88-6, pp. 228, February 2010, INTECH, Croatia, downloaded from SCIYO.COM

to annealing effects of copper selenide nanowire arrays. Finally, section 5 presents a short summary and conclusions.

2.1 Porous alumina

Porous oxide films (alumina) prepared *via* anodization of highly pure and smooth aluminum surface in an aqueous solution of sulfuric, oxalic, and o-phosphoric acid at proper concentration, temperature, and voltage are typical templates for fabrication of arrays of various nanowires in a quite uniform diameter and spacing with well-defined product dimensions at a packing density of 10^9 - 10^{11} species/cm². Recently, highly-ordered structure alumina with a broad range of pore diameters as large as 300 nm (Quin et al. 2005) and as small as 5 nm can be fabricated in an unlimited size area. The pore diameter, cell size, and barrier layer thickness positioned at the bottom of alumina pores (Fig. 1) are all linearly dependent on the anodizing voltage with some exceptions (Jagminas et al. 2001), while the depth of pores is simply controlled by anodizing time (Metzger et al. 2000). According to the final applications the thickness of alumina templates is usually limited to 20-30 μm , but much thicker templates (Römer & Steinem 2004), as well as very thin (Kokonou et al. 2007), are sometimes required.

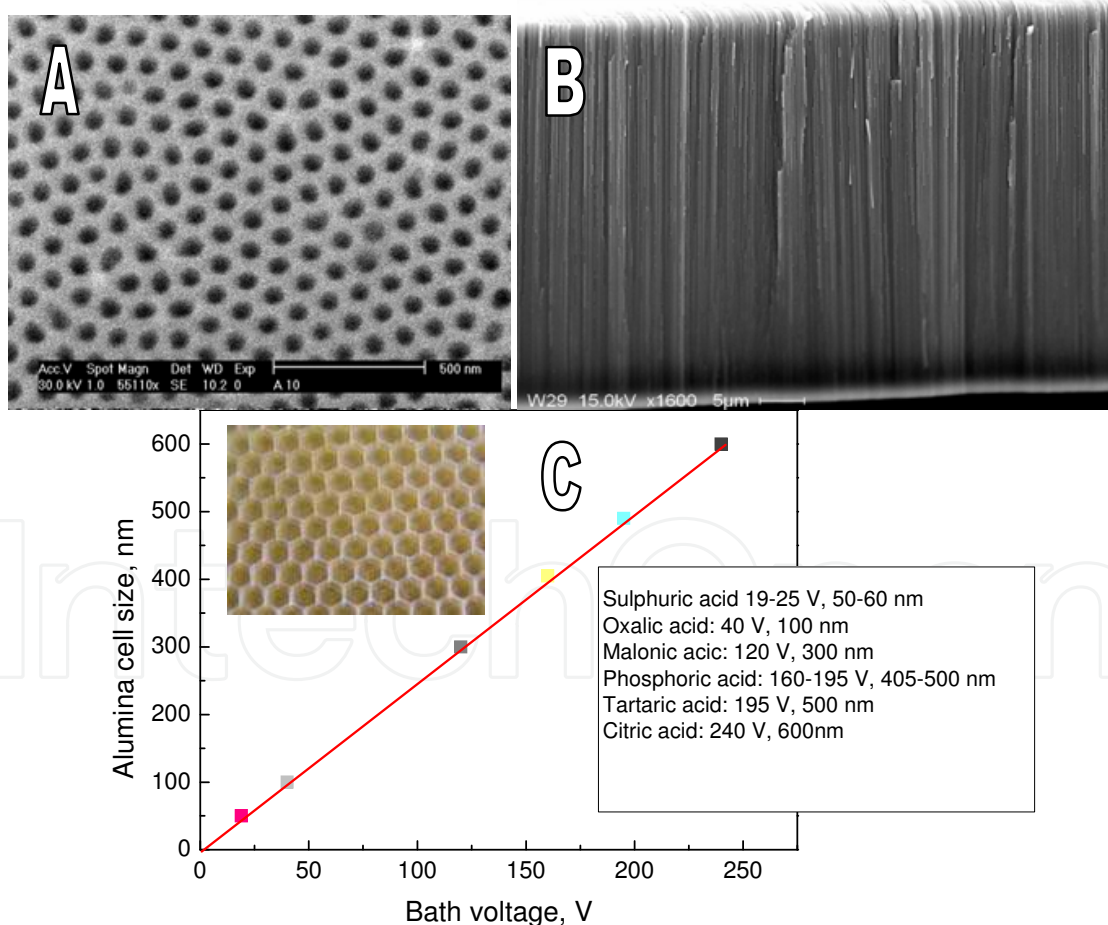


Fig. 1. A typical top-side (A) and cross-sectional (B) SEM view of porous alumina templates. (C) demonstrates variations of alumina cell size on the anodizing voltage for various electrolytes.

The chemical composition of alumina films differs depending on the composition of anodizing solution as well as anodizing conditions due to incorporation of acid anions and water molecules into the outer part of alumina cells. For example, the sulfuric acid alumina films contain high amounts of anionic species (12-14 wt.% sulfate), while the phosphate and oxalate contents in corresponding alumina films are respectively 6-8 and 2-4 wt.% (Thompson 1997). Note that incorporated anion species produce a negative surface charge of the pore walls influencing the pore filling process by one or another material. Therefore, the hydrophobic/hydrophilic pore wall properties play a significant role for nanowire (nanotube) growth in the precursor solution. We suggest that the wettability of pore walls could also influence the nanowire behavior during their storage in the matrix and subsequent treatments, such as annealing (see further).

2.2 Annealing effects in nanowires

Highly-ordered porous aluminas possess quite uniform and parallel nanochannel structure (Fig.1). Therefore, the nanowires loaded within the alumina pores usually possess almost the same diameter as the diameter of pores. The exception here demonstrates nanowires deposited by the pulse current where various diameters of Bi nanowires were obtained *via* variation of the pulse duration (Li et al. 2005). However, in the case of complete filling of the alumina pores, the pore walls that separate the nanowires prevent nanowire diameter variation during high temperature measurements because the thermal expansion coefficient of alumina films is significantly lower ($\sim 8.8 \times 10^{-6} \text{ K}^{-1}$) than that of the metals: Cu ($\sim 2.1 \times 10^{-5} \text{ K}^{-1}$), Ag ($\sim 1.7 \times 10^{-5} \text{ K}^{-1}$), Ni ($\sim 1.7 \times 10^{-5} \text{ K}^{-1}$), Bi ($\sim 1.4 \times 10^{-5} \text{ K}^{-1}$). Thus, at higher heating temperatures the alumina cell walls might produce a radial pressure on the nanowire. As reported (Cai et al. 2008), the radial pressure can be relaxed by the axial expansion if the deposited nanowires are single crystalline demonstrating the complex thermal behavior during annealing in vacuum. In contrast, in the case of polycrystalline nanowires, there are enough of liquid-like spaces between nanocrystallites (Gleiter 2000) to release the stress from the lattice expansion and, thus, the thermal expansion coefficients of such nanowires are almost the same as that of the corresponding bulk.

Wang et al. (2004) claimed that copper nanowires in alumina templates have a thermal expansion coefficient close to zero and this is attributed to the diffusion of vacancy defects from the body to the nanowire surface. The thermal expansion coefficient of Ni nanowires grown within the alumina pores ($\varnothing_{\text{pore}} \sim 60 \text{ nm}$) at -2.0 V by direct current deposition was also studied *in situ* by specimen heating up to 600 °C in vacuum (Cai et al. 2008). These nanowires after deposition were found to be in the polycrystalline state with nanocrystallites up to 40 nm in size. The thermal expansion coefficient of Ni nanocrystallites in the polycrystalline Ni nanowires was estimated to be $1.7 \times 10^{-5} \text{ K}^{-1}$ as in the bulk Ni, enabling to conclude that there is, as well as in bulk Ni, enough space between nanocrystallites to release the stress from the lattice expansion during heat treatment.

The thermal expansion of single crystalline Ag nanowires with the axis direction along the [220] crystallographic direction deposited within the alumina pores ($\varnothing_{\text{pore}} \sim 55 \text{ nm}$) was studied by determining the axial lattice parameter and the state of vacancies in nanowires for the first and repeated annealing in vacuum (Xu et al. 2006). In this study it was shown that the plots of variation of axial lattice parameter for as-grown and annealed silver nanowires can be divided into two regions. When the temperature is below 650 °C for as-grown and 350 °C for annealed specimen, the axial lattice parameter of silver nanowires

keeps nearly constant, but has a slight increase above the indicated temperatures. Thus, the authors concluded that the thermal expansion coefficient of the single crystalline nanowires is determined by two factors: the axial expansion resulted from the radial contraction, which was induced by the surface pressure, and the contraction caused by vacancies. It has also been postulated that after annealing in vacuum the contribution of vacancies to the axial expansion in Ag nanowires decrease due to their congregation into larger voids.

The annealing in vacuum of alumina template, encased with metal alloy nanowire arrays, such as Ag/Cu assembled by nanoparticles of copper and silver, results in the formation of solid solution Ag(Cu) nanowires (Xu et al. 2008). Furthermore, the surface plasmon resonance of Ag nanowires in an average diameter of about 25 nm centered at 410 nm (3.02 eV) red shifted after annealing to ~495 nm (2.50 eV) when the molar ratio of copper to silver increased up to ~40 %.

3. Annealing in air

The heating of alumina templates with nanowires, such as Fe, Cu, FeO(OH) in air can lead to the formation of thermodynamically more stable nanowired metal oxides sometimes demonstrating unique magnetic or optical properties. Also, the annealing procedure has been successfully used for clustering of magnetite, Fe₃O₄, nanoparticles, encased in the alumina template pores by vacuum suction, into nanowires achieving a dramatic effect on their magnetic properties: the coercivity of these arrays at cryogenic temperature increased from 350 to 8000 Oe (Choi et al. 2007).

3.1 Fe nanowire arrays

During recent two decades several works have been reported regarding the electrochemical synthesis of iron nanowires within the alumina pores and their size-dependent magnetic properties (AlMawlawi et al. 1991; Sun et al. 2001; Qin et al. 2005) and corrosion behavior (Jagminas et al. 2008). However, there has been no study trying to fabricate Fe_xO_y nanowire arrays by thermal annealing of embedded iron nanowires within the alumina pores or clarify their transformations during annealing. Thus, in this study we investigated these phenomena as a function of annealing conditions and the size of Fe nanowires by the SEM, XRD and Mössbauer spectroscopies in more detail. In contrast to earlier studies where for electrochemical deposition of iron an aqueous solution composed mainly of iron (II) sulphate and boric acid has been applied, we used a solution of iron (II) sulphate, magnesium sulphate, MgSO₄, and citric acid. We have found that the growth of iron nanowires in this solution under the alternating current mode at a constant average current strength proceeds faster (Fig. 2a) and uniformly (Fig. 2b). The prolonged deposition leads to complete filling of alumina pores and the powdered iron layer formation onto the template surface. X-ray diffraction measurements show only two diffraction peaks for as-deposited material, e.g. a strong peak at 2θ 44.67° and a weak one at 2θ close to 65°. In agreement with the data of the polycrystalline bulk Fe (PDF: No 006-0696), these peaks indicate the formation of metallic α -Fe nanowires with a preferential growth in direction [110] along the crystallographic axes. The decrease in the diameter of alumina pores, $\varnothing_{\text{pore}}$, results in the broadening of diffraction peaks, as expected, without any obvious changes in the growth direction of Fe nanowires (Fig. 3).

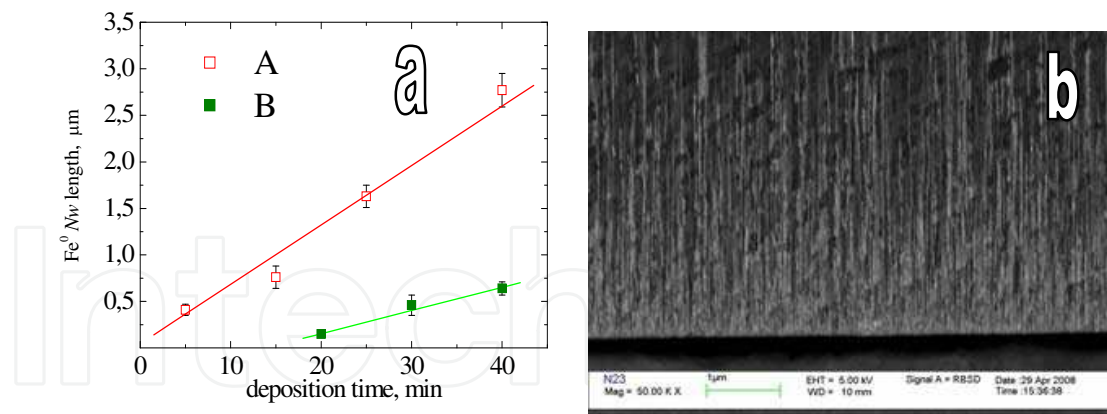


Fig. 2. (a):Variation of average height of Fe nanowires in alumina template pores ($\varnothing_{\text{pore}} \sim 15$ nm) during alternating current (50 Hz) deposition at a constant current density of 0.25 A/dm² from the solution (in M): 0.05 FeSO₄ + 0.025 MgSO₄ + 0.05 citric acid (A) and 0.1 FeSO₄ + 0.7 H₃BO₃ + 0.0085 ascorbic acid (B). (b): A typical cross-sectional FESEM view of alumina template ($\varnothing_{\text{pore}} \sim 28$ nm) encased with Fe nanowires by deposition from (A) solution.

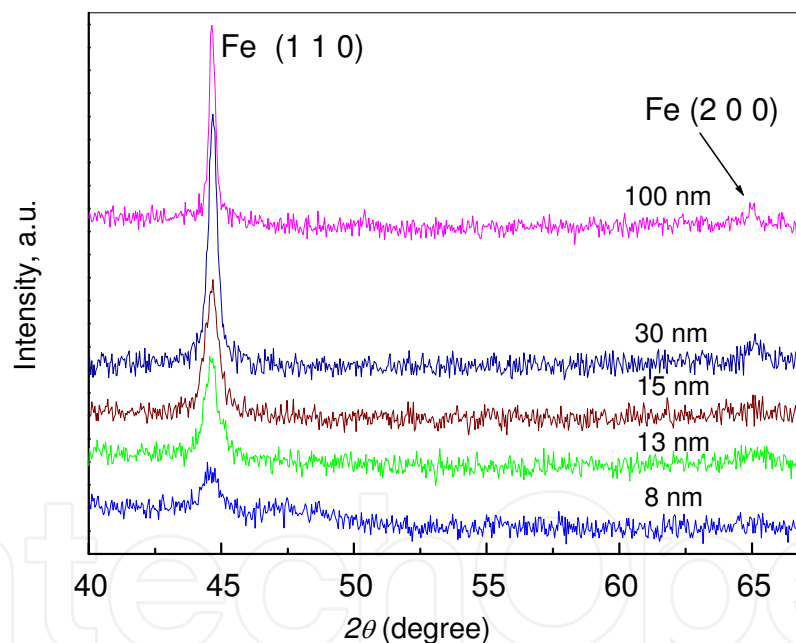


Fig. 3. XRD patterns of alumina films varying the diameter of pores following iron deposition by alternating current in an aqueous solution of 0.1 FeSO₄, 0.025 MgSO₄ and 0.1 M citric acid (pH 2.95) at 0.3 A · dm⁻² and 17 °C for 20-30 min.

The Mössbauer spectra recorded in the conversion electron registration mode from the top and the back-side of alumina matrix, encased with Fe nanowires, after several days storage of not sealed specimen under ambient conditions are shown in Figure 4. As can be seen, these spectra are quite different. A back-side alumina Mössbauer spectrum (Fig. 4b) can be simply fitted using the sextet assignable to ferromagnetic iron, α -Fe. According to (Kuzmann et al. 2003), the ratio of intensities of lines in the Mössbauer spectra sextet is given as:

$$3 : \frac{4 \sin^2 \theta}{1 + \cos^2 \theta} : 1 : 1 : \frac{4 \sin^2 \theta}{1 + \cos^2 \theta} : 3 \quad (1)$$

where θ is the angle between the direction of γ rays and magnetic moments in an iron atom. We have found that for all cases the relative intensities of the second and fifth lines in MS of as-grown Fe nanowires are close to zero, implying that the magnetic moments of the Fe nanowires are along their growth direction. On the contrary, the top-side Mössbauer spectrum recorded for not sealed specimen after several days storage in air demonstrates additionally a typical doublet with the Mössbauer parameters: the isomer shift respectively to α -Fe $\delta = 0.36 \text{ mm s}^{-1}$ and the quadrupole splitting $\Delta = 0.74 \text{ mm s}^{-1}$ assignable to Fe(III). The doublet could arise due to the corrosion and formation of $\text{Fe}(\text{OH})_3$ or $\text{Fe}(\text{OH})_3 \cdot n\text{H}_2\text{O}$ phases. Furthermore, we have determined that the sealing of alumina matrix just after deposition of iron in boiling water protects the Fe nanowires from corrosion during storage of samples under ambient conditions.

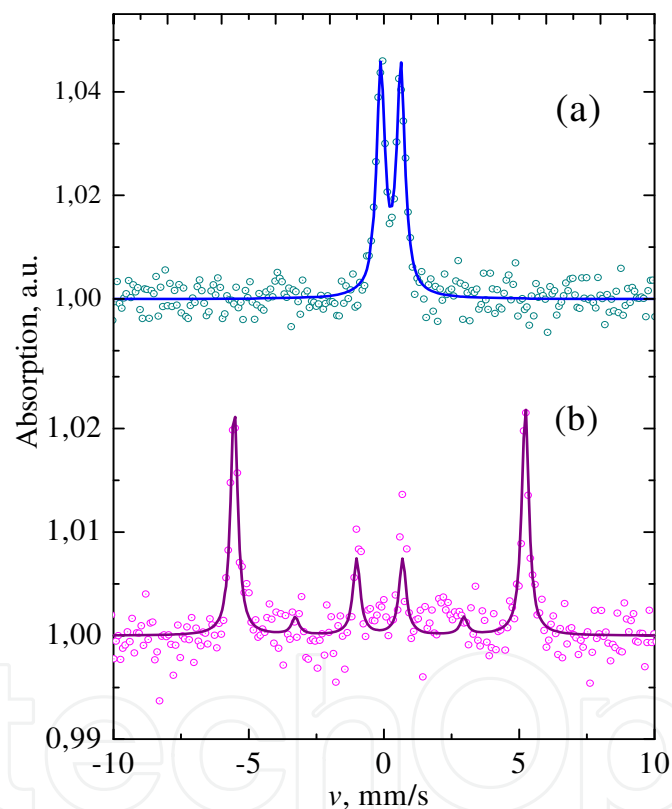


Fig. 4. Mössbauer spectra of alumina template encased with a Fe nanowire array ($\varnothing_{\text{pore}} 15 \text{ nm}$, $l_{\text{Fe}} \sim 7 \mu\text{m}$), taken under the conversion electrons mode from the top (a) and back (b) side of the matrix, indicate that the acmes of iron nanowires corroded forming $\text{Fe}(\text{OH})_3$ or $\text{Fe}(\text{OH})_3 \cdot n\text{H}_2\text{O}$ if alumina after depositions remained unsealed.

Figure 5 shows the XRD spectra of alumina templates with the diameter $\varnothing_{\text{pore}}$ of 15 nm filled with Fe nanowires after annealing. Note that in this experiment the initial weight of analyte and the content of deposited iron were close. As can be seen, the increase in annealing temperature results in the lowering of the content of metallic iron remained after processing. In the case of annealing of the specimens at $450 \text{ }^\circ\text{C}$ for 1.5 hour (curve 3), the peaks of metallic iron in the XRD spectrum of the resulting product disappeared.

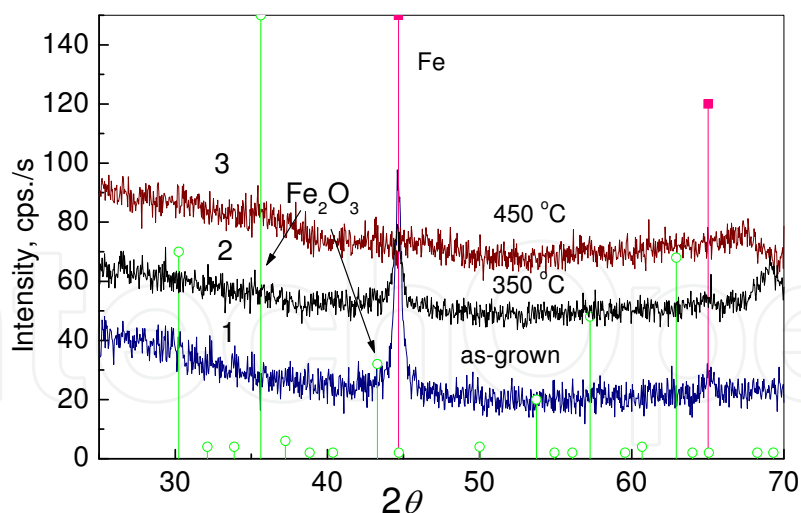


Fig. 5. The XRD patterns of alumina template with encapsulated Fe nanowires by alternating current deposition ($\varnothing_{\text{pore}} 15 \text{ nm}$) following template sealing in boiling water for 30 min (1) and annealing at 300 (2) and 450 °C (3) for 1.5 hour.

The effects of thermal annealing in air on the composition of as-grown Fe⁰ nanowires in sealed alumina pores of a different diameter $\varnothing_{\text{pore}}$ are shown in Figures 6 and 7. All Mössbauer spectra were analyzed by the least squares fitting using the required subspectra and determining the hyperfine parameters, i.e. the isomer shift, δ , the quadrupole splitting, Δ , and the hyperfine field, B . It has been assumed that a relative area of the subspectrum is proportional to the amount of Fe in different compounds. Figure 6a shows a typical Mössbauer spectrum of alumina specimens with a pore diameter of 30 nm after deposition of Fe nanowires and alumina sealing. This spectrum, recorded in the transmission geometry, is of ferromagnetic iron α -Fe fitted using a sextet which has appropriate hyperfine parameters. For Fe nanowires, the parameters were found to be the same as for bulk α -Fe, i.e. the isomer shift $\delta = 0 \pm 0.01 \text{ mm s}^{-1}$, the quadrupole splitting $\Delta = 0 \pm 0.01 \text{ mm s}^{-1}$, the hyperfine field $B = 33.1 \pm 0.1 \text{ T}$ and the line width $\Gamma = 0.28 \pm 0.02 \text{ mm s}^{-1}$. No considerable variation in the hyperfine parameters for different Fe nanowire diameters in the 8 to 30 nm range was obtained.

The annealing of specimens results in the complication of Mössbauer spectra due to transformations of the Fe nanowires composition. These transformations were found to be dependent on the annealing temperature, T_{ann} , and the diameter of pores, $\varnothing_{\text{pore}}$ (Jagminas et al. 2009).

In the case of annealing the Fe⁰ nanowires encased in alumina pores with the diameter $\varnothing_{\text{pore}}$ of 30 nm at $300 \leq T_{\text{ann}} < 600 \text{ }^{\circ}\text{C}$, for example at 400 °C (Fig. 6b), the Mössbauer spectra were fitted with three components, i.e. a sextet demonstrating the presence of ferromagnetic α -Fe and additionally two doublets. These doublets had characteristic Mössbauer spectra hyperfine parameters which can be summarized as follows for all samples: for the first one, the isomer shift $\delta = (0.9 - 1.1) \pm 0.1 \text{ mm s}^{-1}$, the quadrupole splitting $\Delta = (1.9 - 2.3) \pm 0.1 \text{ mm s}^{-1}$ and a line width $\Gamma = (0.3 - 0.7) \pm 0.1 \text{ mm s}^{-1}$ and, for the second one, $\delta = (0.3 - 0.5) \pm 0.1 \text{ mm s}^{-1}$, $\Delta = (0.8 - 1.1) \pm 0.1 \text{ mm s}^{-1}$ and $\Gamma = (0.6 - 0.8) \pm 0.1 \text{ mm s}^{-1}$, respectively. On the basis of Mössbauer spectra parameters the first doublet should be attributed to Fe(II) paramagnetic compound, and can be most probably assigned to the spinel-type FeAl_2O_4 compound (Botta et al., 2003). Moreover, from the large line width of this doublet peaks it

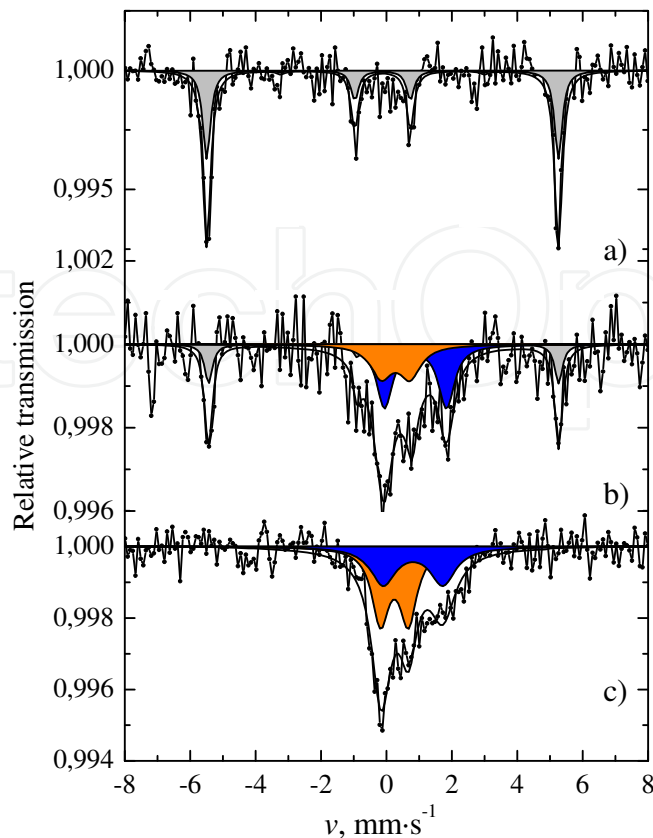


Fig. 6. The Mössbauer spectra recorded in the transmission mode for the Fe nanowires array synthesized within the alumina pores ($\varnothing_{\text{pore}} 30 \text{ nm}$) by alternating current deposition and template sealing in boiling water (a) and annealing at 400 (b) and 600 °C (c) for 1.5 hour.

can be concluded that thermally formed FeAl_2O_4 should be nonstoichiometric. We assigned a second doublet, typical of Fe(III) paramagnetic compounds, to $\alpha\text{-(Fe}_x\text{Al}_{1-x})_2\text{O}_3$ which is obtained when iron incorporates into alumina. As for this component only a paramagnetic doublet is observed, and there are no traces of sextets of iron oxides, x should be below 0.1 (Kuzmann et al. 2003).

The annealing of the Fe nanowire array, encased in the alumina matrix, at $T_{\text{ann}} \geq 600 \text{ °C}$ results in some fading of the black color of alumina. With a further increase in T_{ann} these changes intensified. A typical Mössbauer spectrum of the specimen with the 30 nm diameter after annealing at 600 °C is shown in Figure 6c. In this case, the fitting results revealed a complete transformation of ferromagnetic iron into two components, e.g. FeAl_2O_4 and $(\text{Fe}_x\text{Al}_{1-x})_2\text{O}_3$ with a similar content.

Similar variations in the composition of Fe nanowires upon annealing were determined for iron nanowires encapsulated within the alumina pores with the 15 nm diameter. However, in this case the ferromagnetic component disappeared at about 450 °C as a result of full transformations into paramagnetic Fe(II) and Fe(III) components with a somewhat higher amount of Fe(III). It is noteworthy that with a further increase in T_{ann} the ratio between Fe(III) and Fe(II) components changes significantly. For example, after annealing at 600 °C the resultant products contain ~ 80 % of Fe(III) and only about 20 % of Fe(II).

The compositional investigations of Fe nanowires encased within the alumina template pores with the 13 nm diameter, produced by alternating current deposition under the

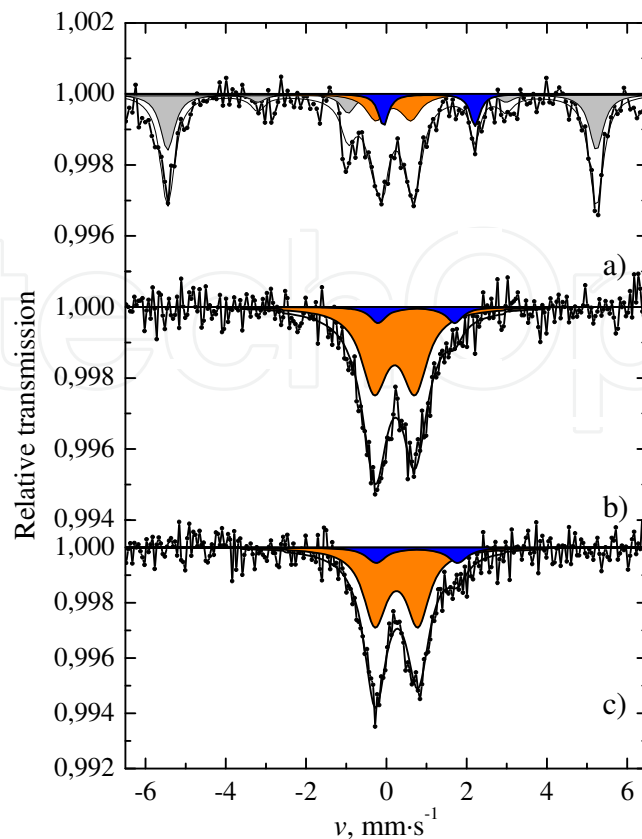


Fig. 7. The Mössbauer spectra recorded in the transmission mode for the Fe nanowires array in the alumina template with an average pore diameter of 8 nm after sealing (a) and annealing at 400 (b) and 510 °C (c) for 1.5 hours. To increase sensitivity of measurements, the deposition solution additionally contained 0.5 g · dm⁻³ of ⁵⁷Fe.

conditions of this study, revealed two additional features (see Fig. 8c). Firstly, some part of deposited iron within the alumina pores even before annealing was found to be in the form of paramagnetic Fe(III) implying that the formation of (Fe_xAl_{1-x})₂O₃ is possible as a result of the alumina template sealing in boiling water. Secondly, in the case of the 13 nm diameter template, a ferromagnetic component disappeared in the vicinity of 400 °C being transformed fully into paramagnetic Fe(III) and Fe(II) components in proportions similar to a case of 15 nm diameter template annealed at 600 °C.

The Mössbauer spectrum of alumina template with an average diameter of 8 nm filled with iron nanowires even after the sealing (Fig. 7a) was found to be more complicated and composed of three components similar to those following the annealing of specimens with $\varnothing_{\text{pore}} \geq 15$ nm. The quantities of paramagnetic Fe(III) and Fe(II) components were found to be larger making up together more than 40 % of the total amount of deposited iron (Fig. 8d). Moreover, annealing of these specimens results in more rapid transitions of ferromagnetic Fe(0) to paramagnetic Fe(III) and Fe(II) compounds at obviously lower temperatures with prevailing Fe(III) formation.

The results obtained indicate that the diameter of primary iron nanowires is a key parameter which determines the transformations when annealing at the same temperature. These transformations became especially obvious even at ~100 °C if the nanowires diameter is in

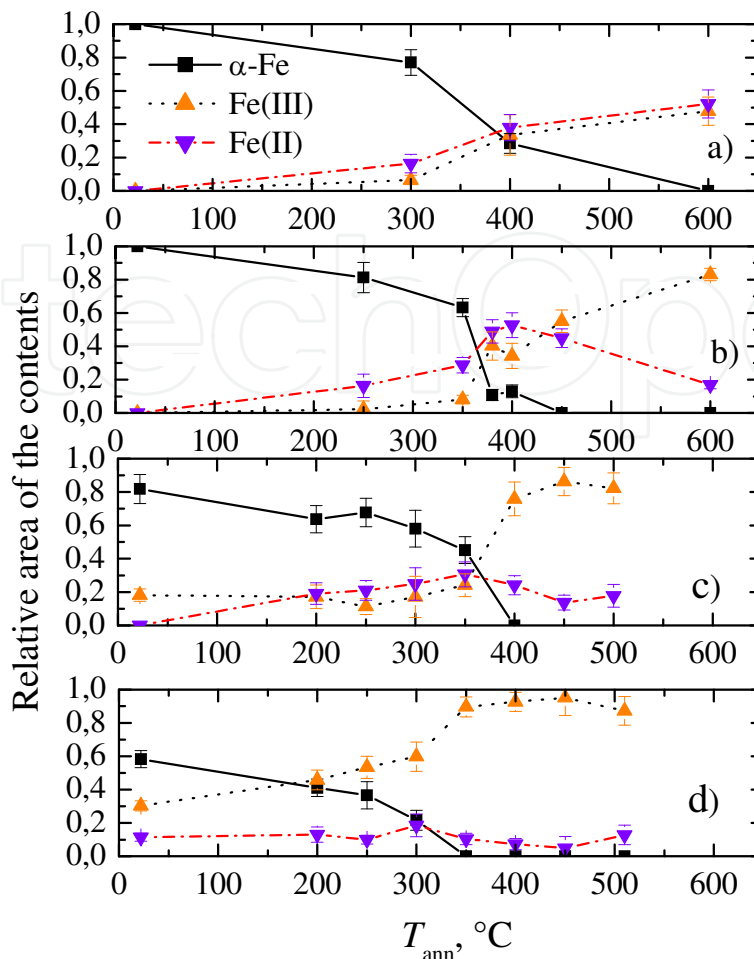


Fig. 8. Dependences of the amount of iron phases formed within the alumina template pores *via* alternating current deposition and annealing on the annealing temperature and the average pore diameter (in nm): (a) 30; (b) 15; (c) 13 and (d) 8.

the order of the Debye length. We suggest that this effect is linked to the increase in a free surface energy impact of thin nanowires modifying the temperature of thermal diffusion of material molecules into alumina bulk.

3.2 Sn nanowire arrays

Due to chemical stability and a wide band gap at room temperature [3.6-4.0 eV (Ji et al., 2004)] SnO_2 thin films are promising materials for solar cells (Ferrete et al. 1997), short wavelength optoelectronic (Song et al., 2004), and blue photoluminescence (Presley et al. 2004) devices. Besides, tin-based oxides are promising candidates to replace the carbon-based anode materials because of their large capacity for lithium insertion by the formation of $\text{Li}_{4.4}\text{Sn}$ alloy (Wang et al. 2005). During the recent decade SnO_2 nanotubes (Qin et al. 2008), nanoparticles and nanorods (Firooz et al. 2008), and nanobelts (Fujihara et al. 2004) have been fabricated by different methods such as sol-gel process (Gu et al. 2003), hydrothermal synthesis (Firooz et al. 2008; Fujihara et al. 2004), chemical vapour deposition (CVD) (Kong et al. 2003; Sundqvist et al. 2006), metalorganic chemical vapour deposition (MOCVD) (Feng et al. 2008), and etching of tin foils in alkaline solution (Peng et al. 2008). Despite these proposals there is a great need to develop reliable and cheap synthesis

methods for fabrication of densely-packed, uniform-shaped tin oxide nanowire arrays for practical applications.

Here we report the way for fabrication arrays of the core (SnO)/shell (SnO₂) barbed-shaped nanowires *via* electrochemical formation of densely-packed tin nanowires inside the alumina pores and their subsequent heat treatment in air at a proper protocol. The morphology of Sn nanowire arrays fabricated within alumina pores was investigated before and after heat treatments using field emission scanning electron (FESEM) and transmission electron (TEM) microscopy in alumina cross-sections followed by a complete template dissolution. Mössbauer spectra were recorded in a constant acceleration mode using a spectrometer Wissenschaftliche Elektronik GMBH and an ¹¹⁹CaSno₃ source. The velocity scale was calibrated relative to CaSnO₃. All experimental spectra were fitted to Lorentzian lines using a least-squares fitting algorithm.

Good uniformity and completeness of alumina pores filling by tin nanowires in the solution containing SnSO₄, tartaric acid, C₄O₆H₆, hydrazine sulphate, and H₂SO₄ by alternating current deposition can be evidenced from the FESEM images of alumina templates in their cross-sections (Fig. 9A) and after the following template etching (Fig. 9B). We found that annealing of these specimens results in the change of alumina black colour towards puce and gold tints, as well as the decrease in Sn⁰ diffraction peaks and the appearance and growth of new ones with increase in annealing temperature, T_{ann} . The first diffraction peaks of SnO₂ appeared for samples annealed at 400 °C. Note that all peaks attributable to metallic tin disappeared only for $T_{\text{ann}} \geq 500$ °C, e.g. at a temperature much higher than the melting point of bulk tin (231.9 °C). In this case, the diffraction lines at $2\theta = 26.58, 33.87, 51.76^\circ$ can be assigned to tetragonal rutile-type crystalline phase of tin(IV) oxide, SnO₂ (PDF file no. 41-1445).

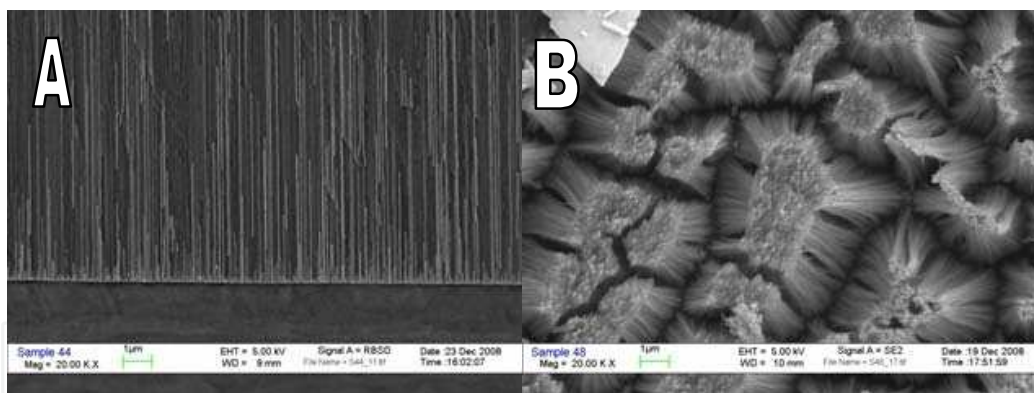


Fig. 9. A typical cross-sectional (A) and in-plane (B) FESEM view of alumina templates encased with tin nanowires by alternating current deposition from the solution (in M): 0.05 SnSO₄, 0.03 tartaric acid, 0.015 hydrazine sulfate and sulfuric acid (pH = 1.15) at a constant average current density of 2.75 mA cm⁻² for 30 min. Pore diameters are 15 (A) and 28 nm (B). The alumina in (B) is partially dissolved.

In the case of a 2 hour long annealing at 500 °C of the templates with pore diameters of 15 nm, the crystallite size of SnO₂ particles calculated from the XRD line broadening using TOPAS software, based on the Rietveld structure refinement Scherer equation, is about 9.7 ± 1.5 nm. It is worth noticing that the XRD pattern of specimens treated at 450 °C, except the diffraction lines attributable to SnO₂, contained additional lines whose positions depend on the annealing time, τ_{ann} . These lines could be assigned to the crystalline phase of Sn(II)

oxide, SnO (PDF file no. 06-0395) (Fig. 10). Nevertheless, the peak positions of these lines were found to be slightly shifted towards lower values of diffraction angles, indicating the distortion of crystalline lattice, since $a = 3.802$ and $c = 4.900$ Å instead of $a = 3.802$ and $c = 4.836$ Å.

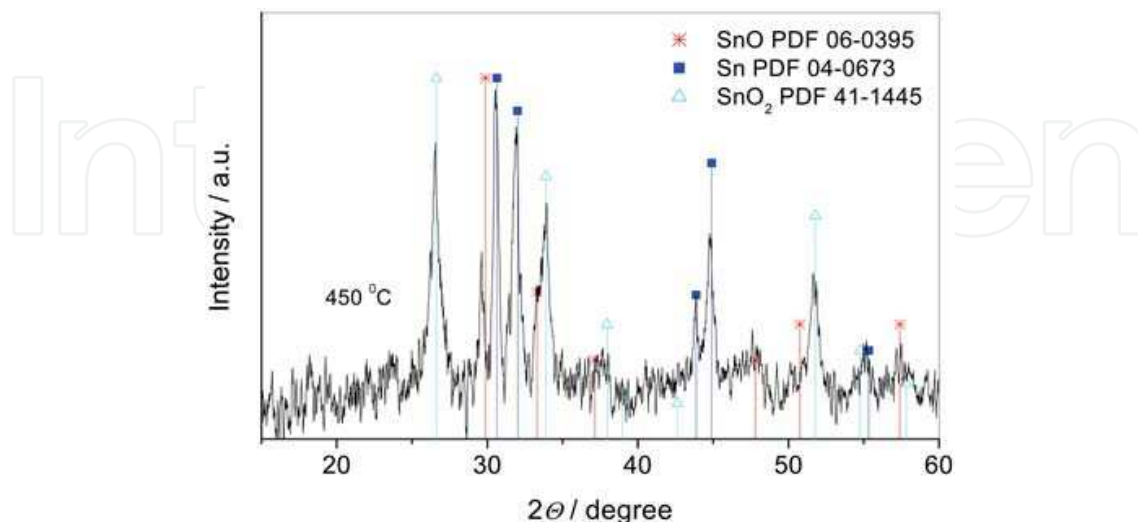


Fig. 10. X-ray diffraction pattern of alumina template encased with tin nanowires ($\varnothing_{\text{Sn}} \sim 15$ nm) by deposition from the solution as in Fig. 9 at the average current density (50 Hz) of 2.75 mA cm^{-2} for 30 min after annealing at 450 °C for 3 hours.

To qualitatively and quantitatively further assess the effect of annealing on the transformation of Sn^0 nanowires, encased within the alumina pores by electrodeposition, Mössbauer spectroscopy was performed and a typical Mössbauer spectrum of the annealed products is presented in Figure 11a. In the case of as-deposited nanowired material, a singlet line in Mössbauer spectrum with the isomer shift, δ , equal to 2.49 ± 0.02 mm/s, attributable to $\beta\text{-Sn}$, can be only observed.

Our investigations revealed that after alumina template sealing in boiling water and annealing the Mössbauer spectrum of Sn nanowires loaded inside alumina pores changes drastically. In the case of annealing the specimen at $T_{\text{ann}} \geq 450$ °C, the resulting Mössbauer spectrum is composed of two broadening doublets characteristic of SnO and SnO₂ (Fig. 11a). The quadrupole splitting (Δ) and isomer shift (δ) values for Sn²⁺ and Sn⁴⁺ states in annealed specimens are presented in Table 1. However, the magnitude of these parameters coincides with the well known ones only for the crystalline SnO₂ (Collins, et al. 1979). For SnO, in all annealed specimens both Δ and δ values obtained are larger than those for stable tetragonal (black) SnO powder, as can be seen in Fig. 11 and Table 1. We suppose that differences in SnO parameters are due to the formation of nanocrystalline nonstoichiometric form of tetragonal SnO with possible contribution of amorphous SnO as an intermediate oxide phase through the sequence of reactions: $\text{Sn}^0_{\text{s}} \Rightarrow \text{Sn}^0_{\text{liq}} \Rightarrow \text{SnO}_{\text{amorph}}(\text{SnO}_{\text{cryst}}) \Rightarrow \text{SnO}_2$.

Notably, an increase in T_{ann} up to 550 °C results in a decrease in the SnO content. For example, in the case of annealing at 450 °C, the content of remained SnO was 1.75 times larger than that at 500 °C.

Typical transmission electron microscopy images on SnO/SnO₂ blend are depicted in Fig. 12. First, we see that Sn^0 rod-shaped nanowires transform into barbed-type nanowire products upon heat treatment. We also see that the barbed nanowires are 2 or 3 times

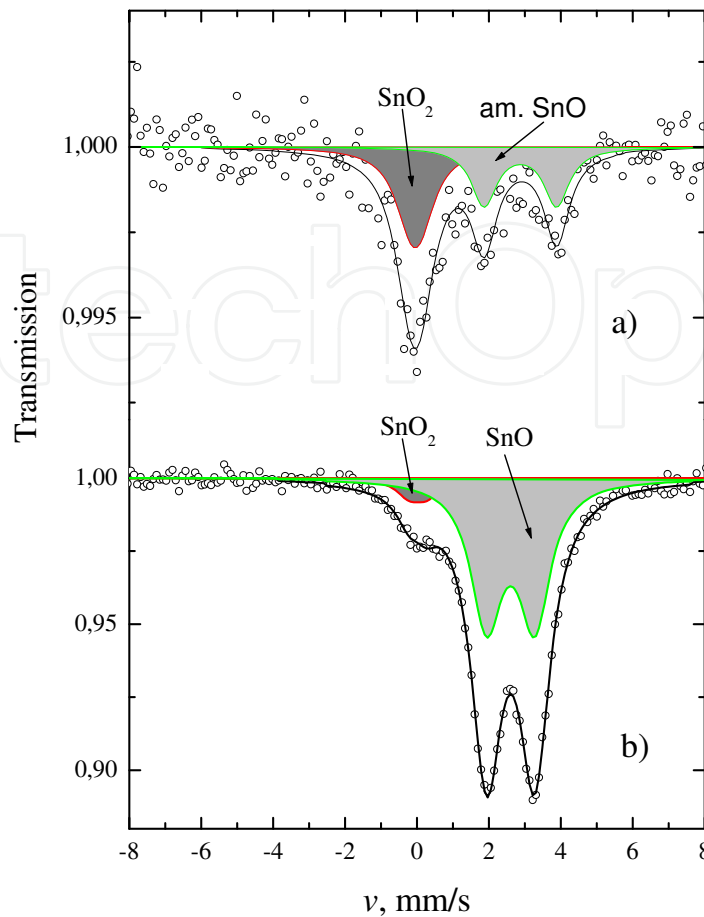


Fig. 11. Room temperature ^{119}Sn Mössbauer effect spectrum of Sn^0 nanowires array fabricated in the pores of alumina template by electrodeposition as in Fig. 10 after 2 hours annealing at $450\text{ }^\circ\text{C}$ (a) and the same spectrum for commercial SnO powder (b).

Sample	$\beta\text{-Sn}$		SnO			SnO_2		
	δ , mm s^{-1}	Γ , mm s^{-1}	δ , mm s^{-1}	Δ , mm s^{-1}	Γ , mm s^{-1}	δ , mm s^{-1}	Δ , mm s^{-1}	Γ , mm s^{-1}
As-deposited.	2.49 ± 0.02	0.94 ± 0.05	—	—	—	—	—	—
Annealed $450\text{ }^\circ\text{C}$, 2 h.	—	—	2.88 ± 0.04	2.02 ± 0.07	0.86 ± 0.04	-0.05 ± 0.03	0.3 ± 0.2	1.0 ± 0.2
Annealed at $500\text{ }^\circ\text{C}$ 2h	—	—	2.87 ± 0.05	2.08 ± 0.09	0.86 fixed	0.02 ± 0.01	0.62 ± 0.02	0.88 ± 0.05
Annealed at $500\text{ }^\circ\text{C}$, 2h, (160 K MS)	—	—	3.18 ± 0.05	2.38 ± 0.09	0.95 ± 0.17	0.09 ± 0.02	0.69 ± 0.03	0.87 ± 0.06
Tetr. SnO sample	—	—	2.60 ± 0.01	1.34 ± 0.01	1.06 ± 0.01	0.02 ± 0.04	0.5 ± 0.1	0.83 ± 0.15

Table 1. The parameters of Mössbauer spectra for Sn^0 nanowire arrays annealed at indicated temperatures when the template pore diameter is 15 nm.

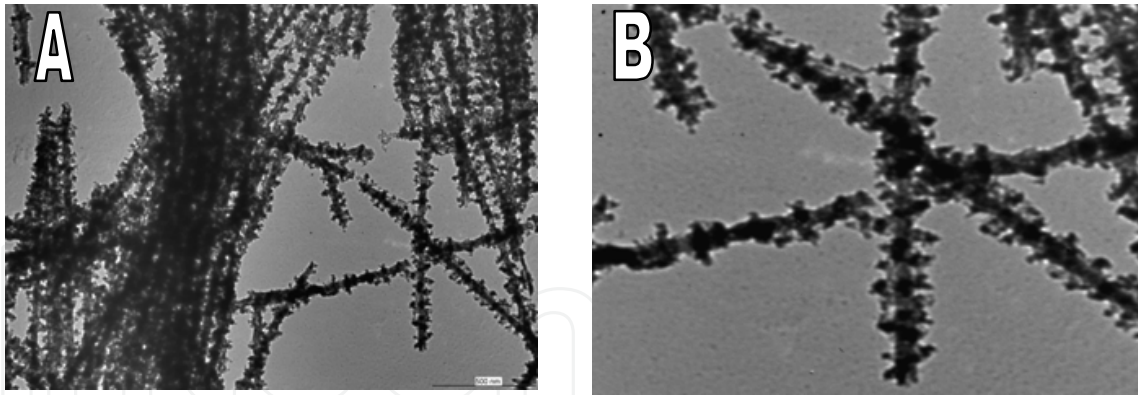


Fig. 12. Typical TEM images of SnO/SnO₂ barber-shaped nanowires released from the support. $\varnothing_{\text{pore}} = 28$ nm. Sn⁰ nanowire array in a sealed alumina template was heat treated at 500 °C in air for 2 hours.

thicker at the thorn sites. To the best of our knowledge, such a previously unthinkable architecture of nanowires has never been seen in nanotechnology. Especially interesting is the formation of numerous mechanically quite stable thorns. It is assumed that these thorns of up to 25 nm height (for 28 nm pore template) are composed of crystalline SnO₂ as more energetically favourable. We suggest that these thorns grow up through the all-out thermal and pressure induced diffusion of molten tin inside the walls of alumina nanochannels and that oxygen-bondings result in strong compression and distortion of the matrix cells, thereby destroying the matrix due to increase in size and shape of a novel nanowired product.

3.3 α - and γ -Fe₂O₃ composite nanowire arrays via electrodeposition and thermal decomposition of lepidocrocite, γ -FeOOH

Highly-ordered, uniform and densely-packed arrays of iron oxide nm-scaled architectures, such as nanowires and nanotubes, receive considerable attention due to their prospective use in solar cells, gas sensing and super-high-density recording devices. Magnetite, Fe₃O₄, maghemite, γ -Fe₂O₃, and hematite, α -Fe₂O₃, are the crystallographic materials of iron oxides differing in structure and properties. Magnetite and maghemite are ferromagnetics while bulk hematite is anti ferromagnetic material with the Neel temperature 950 K and Morin transition temperature 263 K (Cornell & Schwertmann 1996). Note that composites from mixed iron oxides due to magnetic exchange coupling between magnetic particles frequently demonstrate a shift of hystereses and coercivity (Christensen et al., 1982) currently paving a way to their relevant applications in catalysis, high density recording contours, and biomedical diagnostics (Blanc-Beguin et al. 2009).

Bulk ferromagnetic maghemite is a form of iron oxide that can be obtained by thermal decomposition of lepidocrocite, γ -FeOOH (Özdemir & Dunlop 1993). γ -Fe₂O₃ is a transition form, and upon further heating undergoes a sequence of phase transformations up to hematite, α -Fe₂O₃ (Gehring & Hofmeister 1994). On the whole, the temperature at which dehydroxylation reaction begins depends on the preparation and heating conditions of bulk lepidocrocite crystals (Morales 1998). Thus, the activation energy of this reaction varies from 13.1 to 26.7 kcal mol⁻¹, depending on the crystallinity of γ -FeOOH.

The thermal decomposition of iron oxyhydroxide polymorphs, such as goethite, α -FeOOH, akaganeite, β -FeOOH, lepidocrocite, and amorphous FeOOH · nH₂O has always been an interesting subject seeking to form Fe₃O₄ and α -, γ -, or ϵ -Fe₂O₃ materials and their composites.

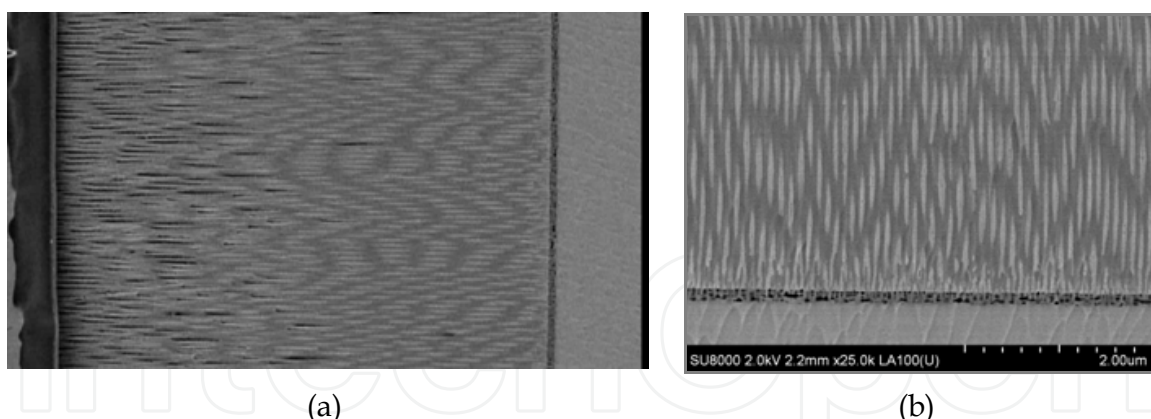


Fig. 13. Cross-sectional FESEM view of alumina templates loaded with lepidocrocite nanowires by alternating current (50 Hz) deposition from 0.022 M $\text{Fe}(\text{NH}_4)_3(\text{C}_2\text{O}_4)_3$ and 0.011 M $^{57}\text{Fe}(\text{C}_2\text{O}_4)_3$ kept at pH 5.75. $\varnothing_{\text{pore}}$: (a) 45 nm, (b) 150 nm.

However, to date only akaganeite nanowires have been successfully encased within the alumina pores by electrodeposition (Gao et al. 2002; Zhang et al. 2007) transforming them later to hematite nanowires by heat treatment in air at $T_{\text{ann}} \geq 500$ °C. Recently we have developed a route for uniform synthesis of amorphous lepidocrocite nanowires within the alumina pores using an alternating current mode (50 Hz) and an aqueous solution of iron(III) ammonium oxalate friendly to alumina matrices (Jagminas et al. 2009b). A nice filling of alumina pores with lepidocrocite nanowires in this solution by deposition through the barrier layer at a constant alternating current density of 0.35 A dm^{-2} was evidenced here both for 45 and 150 nm $\varnothing_{\text{pore}}$ templates looking at the parts (a) and (b) of Fig. 13, which show the FESEM images taken from the template cross-sections. This is also evidenced by uniform colouring of alumina matrices in deep orange tints. Again, the growth of lepidocrocite nanowires was determined here using the Mössbauer spectra at cryogenic temperatures (Fig.14) and $^{57}\text{Fe}(\text{C}_2\text{O}_4)_3$ precursor.

The set of Mössbauer spectra for $\gamma\text{-FeOOH}$ nanowires encased in the alumina template with $\varnothing_{\text{pore}} \sim 45$ nm and heat-treated at temperatures from 150 to 650 °C for 3 hours ($\partial T/\partial t = 10$ °/min) is shown in Fig. 15. There the group of spectra recorded at room temperature is labeled by (a) while (b) shows a similar spectra recorded at a low temperature. The first clear feature from Fig. 15 is that lepidocrocite nanowires remain quite stable up to 400 °C although the color tint of alumina templates after annealing at $T_{\text{ann}} \geq 150$ °C changes evidently. In line of these observations it has been found that quadrupole splitting of Mössbauer spectra doublet, attributable to $\gamma\text{-FeOOH}$, increases with annealing temperature likely due to elimination of the absorbed and of the molecular water as in the case of akaganeite ($\beta\text{-FeOOH}$) calcination (Gao et al. 2002).

Noteworthy that the sextets, attributable to Fe_2O_3 phases appear only for specimens heat-treated at $T_{\text{ann}} \geq 500$ °C. In fact, the heat treatment at 500 °C results in the largest Mössbauer spectra changes of the product deposited in alumina pores; with a further temperature increase these changes become less pronounced. Thus, in the next setup we analyzed the composition of the specimen calcinated at 500 °C in more detail using both room and low temperature Mössbauer spectra. The results obtained are presented in Fig. 16. To fit these spectra, we used up to two sextets and one-two doublets. The sextets were ascribed to the hematite with a hyperfine field of ~ 50.1 T at room temperature and to Fe_2O_3 with hyperfine field of ~ 47.9 T. Again, doublets were ascribed to the species in a superparamagnetic state

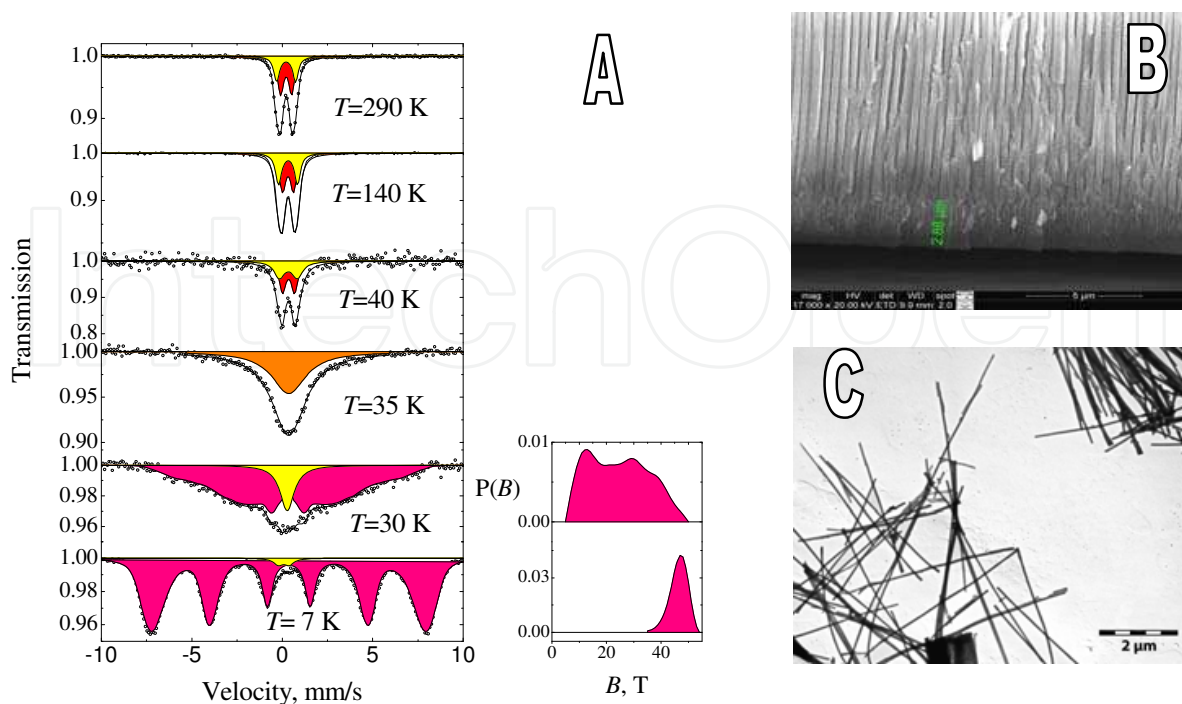


Fig. 14. The transmission Mössbauer spectra taken at indicated temperatures show the magnetic transition below 35 K for as-deposited FeOOH nanowires inside the alumina pores (B,C) implying the formation of quite pure γ -FeOOH phase. The right side in (A) shows the hyperfine fields distribution for description of the spectra.

and/or to paramagnetic irons. The refined spectral parameters are listed in Table 2. From the analysis of these data the presence of hematite phase in the annealed specimen is clear. Furthermore, the low temperature measurement in Fig. 15 proved that a part of the doublets correspond to superparamagnetic particles of γ -Fe₂O₃ whereas the rest can be assigned to the paramagnetic phase of maghemite, γ -Fe₂O₃. Note that formation of superparamagnetic species demonstrates the increase of the central part in the low temperature Mössbauer spectra. This increase can be due to the existence of small species of hematite as well as due to maghemite. Two subspectra in the low temperature spectrum split part are characteristic by different quadrupols. Without any doubt one of them ($\Delta = 0.37$ mm/s), typical at a temperature lower than Morin temperature, T_M , is related by the presence of hematite. The second one with $\Delta = 0.04$ mm/s, as an intermediate value close to zero, could be attributed either to γ -Fe₂O₃ or to very small particles of hematite in which the Morin transformation effect, similar to that as in the case of (Schroerer & Nininger 1967), might take place.

By the analogy with the thermal decomposition of lepidocrocite in a colloidal state (Gendler et al., 2005), it is thought that the transformation reaction γ -FeOOH \Rightarrow γ -Fe₂O₃ \Rightarrow α -Fe₂O₃ in nanowired amorphous lepidocrocite, γ -FeOOH \cdot nH₂O, proceeds *via* a sequence of several steps. The first one, associated with desorption of physisorbed molecular water, takes place even at T_{ann} around 150 °C, because the color and optical properties of alumina templates loaded with lepidocrocite nanowires evidently change under these conditions. This observation is in line with the indication (Gehring & Hofmeister, 1994) that, on the

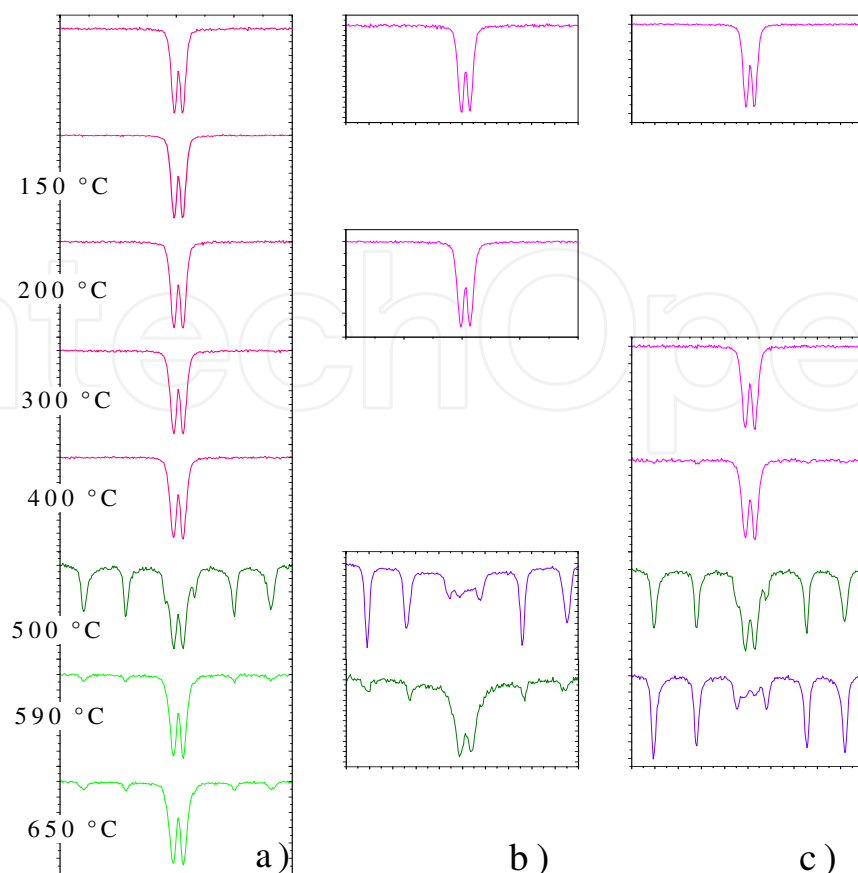


Fig. 15. The transmission Mössbauer spectra taken at room (a, c) and 140 K (b) temperatures for lepidocrocite, γ -FeOOH, nanowire arrays heat treated at indicated temperatures for 3 hours. $\varnothing_{\text{pore}}$: (a, b) 45 nm, (c) 150 nm.

molecular level, the removal of OH groups in the lepidocrocite begins at 142-155 °C. Based on the results obtained here by Mössbauer transmission spectroscopy and Raman scattering (not shown here) it seems likely that the second step, corresponding to the dehydroxylation of iron oxyhydroxide nanowires to γ - and α -Fe₂O₃, completely proceeds in the vicinity of 500 °C although from literature data (Bernal et al. 1957) the rhombic structure of synthetic lepidocrocite reconstructs to cubic maghemite in the 230-250 °C region which at 375 °C is transported completely to hematite with a hexagonal structure, e.g. at much lower temperatures.

4. Annealing effects of copper selenide nanowire arrays

The formation of copper selenide nanowire arrays, in particular those of Cu_{2-x}Se and Cu₃Se₂ within alumina pores has been demonstrated by us in an aqueous solution of CuSO₄, MgSO₄ and H₂SeO₃ at proper concentrations and pH by alternating current deposition (Jagminas et al. 2006). However, only an almost pure phase of Cu_{1.75}Se showing both a direct energy bandgap, $E_{g,\text{dir}}$, of about 2.3 eV and a defect related optical absorption band close to 1.1 eV, has been deposited using sulfuric acid alumina templates with an average pore diameter, $\varnothing_{\text{pore}}$, of 15 nm. One should note that such values are close to those reported for Cu_{1.85}Se thin films where $E_{g,\text{dir}} = 2.2$ eV and $E_{\text{def}} = 1.4$ eV (Herman & Fabrick 1983). Very recently, the optimal composition for the deposition of a quite pure phase Cu₃Se₂ nanowires inside the

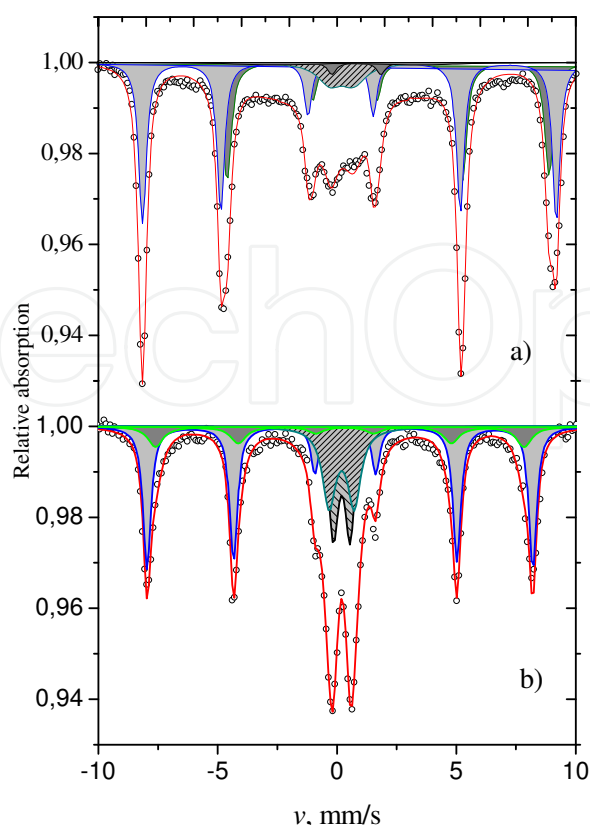


Fig. 16. The transmission Mössbauer spectra recorded at 140 K (a) and room (b) temperatures for lepidocrocite nanowire arrays loaded inside the alumina matrix ($\varnothing_{\text{pore}} 45$ nm) after heat treatment at 500 °C in air for 2 hours.

		$S, \%$	$\delta, \text{mm/s}$	$\Delta, \text{mm/s}$	B, T	A_{23}
Room temperature	1	37	0.37 ± 0.01	-0.22 ± 0.01	50.1 ± 0.1	2.83 ± 0.06
	2	19	0.36 ± 0.01	-0.21 ± 0.02	47.9 ± 0.2	2.45 ± 0.18
T=140 K	1	39	0.47 ± 0.01	0.37 ± 0.01	53.7 ± 0.1	2.81 ± 0.06
	2	37	0.49 ± 0.01	0.04 ± 0.01	52.8 ± 0.1	3.13 ± 0.07

Table 2. Calculated parameters of Mössbauer spectra sextets (Fig. 16) for 45 nm diameter lepidocrocite nanowire array heat treated at 500 °C for 2 hours.

alumina pores has also been reported (Jagminas et al. 2009c). Furthermore, it has been demonstrated that nm-sized crystals and nanowires of $\text{Cu}_{1.75}\text{Se}$ and Cu_3Se_2 encased in the transparent alumina template demonstrate nonlinear absorption features at $1.06 \mu\text{m}$ (Statkutė et al. 2008; Juška, et al. 2009a). We have found that Cu_3Se_2 /alumina greenish tints, characteristic of these films, upon its annealing in ambient atmosphere even at a moderate temperature of 150 °C became yellow. Upon further increase in annealing temperature, these changes became more obvious.

Figure 17 presents the XRD profiles of the alumina templates filled by Cu_3Se_2 nanowires before and after annealing for three hours at various temperatures. An as-deposited material pattern shows twelve well-defined peaks with relative intensities completely consistent with those of crystalline tetragonal Cu_3Se_2 [$a = 4.27 \text{ \AA}$ and $c = 6.40 \text{ \AA}$ (PDF 47-1745), umangite]. The thermal treatment in air of a Cu_3Se_2 nanowire-shaped material results in decomposition

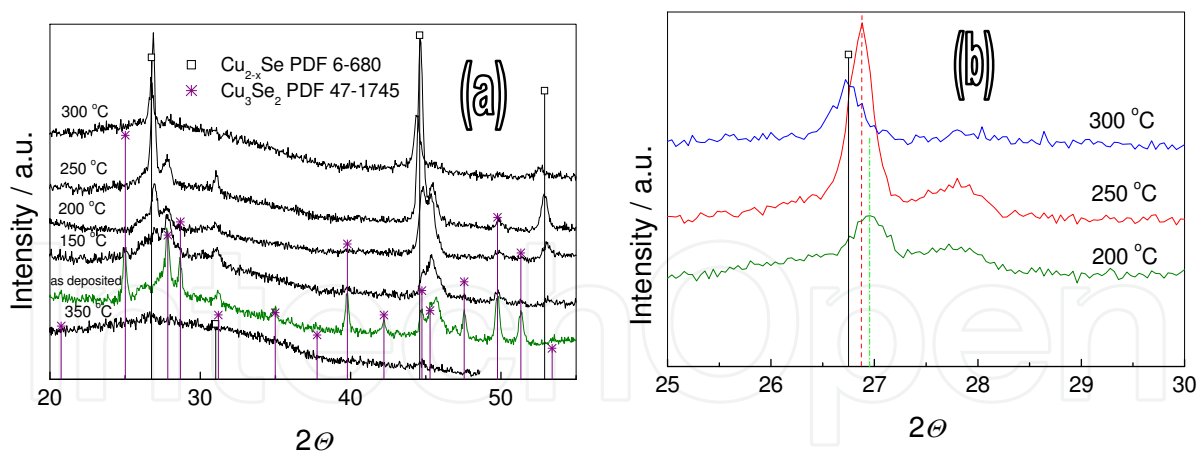


Fig. 17. (a) XRD patterns of alumina matrices encased with copper selenide by alternating current deposition in the solution (in M): 0.03 CuSO_4 , 0.015 H_2SeO_3 , 0.03 $\text{Al}_2(\text{SO}_4)_3$, 0.005 triethanolamine, and H_2SO_4 (pH = 1.15) at 0.5 A dm^{-2} for 45 min before and after annealing in air for one hour. (b) XRD pattern fragments within a 25 to 30° 2θ range for the same as in (a) Cu_3Se_2 /alumina specimen annealed at 200, 250 and 300°C .

of copper selenide depending on T_{ann} . At $T_{\text{ann}} \approx 200^\circ\text{C}$ a part of Cu_3Se_2 transforms into Cu_{2-x}Se . With further increase in the annealing temperature the amount of Cu_{2-x}Se component increases becoming dominant at $\sim 300^\circ\text{C}$. The most significant fact is the stoichiometry of Cu_{2-x}Se phase found to be also dependent on T_{ann} , as judged from the diffraction peak position in the XRD pattern fragment within the range of 2θ from 26.5 to 27.5° (Fig. 17b). We have found that annealing of nanowire-shaped Cu_3Se_2 at 250°C results in formation of $\text{Cu}_{1.85}\text{Se}$, while annealing at lower, e.g. 200°C , or higher, e.g. 300°C , temperatures yields Cu_{2-x}Se with $x > 0.15$ and $x < 0.15$, respectively. This effect possibly originates from the diffusion of selenium into the alumina bulk upon heating.

Transmission spectra of alumina templates encased with almost pure Cu_3Se_2 nanowires before and after annealing at various temperatures were recorded for wavelengths ranged from 190 to 3125 nm (Fig. 18a). It is obvious that the shape of absorption spectrum for as-deposited Cu_3Se_2 nanowires array (curve 1) differs from the ones annealed (curves 2-5). The main feature of the first is a wide absorption band in the visible and near infrared starting just below the edge of a fundamental band gap and covering almost the whole dip of the spectra. Analysis performed on this part of absorption spectra (see Figure 18b) revealed two Lorentzians $\{w / (4(h\nu - h\nu_0)^2 + w^2)\}$ superimposed, each of them with peaks at energy $h\nu_0 = 1.14$ and 1.65 eV with FWHM - $w = 0.58$ and 1.48 eV , respectively. These results suggest that along with Cu_3Se_2 another selenide, like Cu_{2-x}Se in the amounts undetectable for XRD, takes part in the absorption.

Band gap energy (E_g) values of deposited and annealed products were calculated using: $\alpha(h\nu) = A(h\nu - E_g)^{n/2}$, where α is the absorption coefficient, A is a constant, E_g is the band gap value, $h\nu$ is the photon energy and n is dependent on the nature of transition: 1 or 3 for direct and 4 or 6 for indirect transitions. This estimation gives that direct band gap values ($E_{g,\text{dir}}$) for as-grown and annealed specimens increase with annealing temperature from $\sim 2.16 \text{ eV}$ (before annealing) to 2.44 eV ($T_{\text{ann}} = 300^\circ\text{C}$).

Optical nonlinearities of as-grown and thermally treated specimens were studied in the experimental set-up based on the mode-locked Nd:glass laser (the wavelength of 1053 nm,

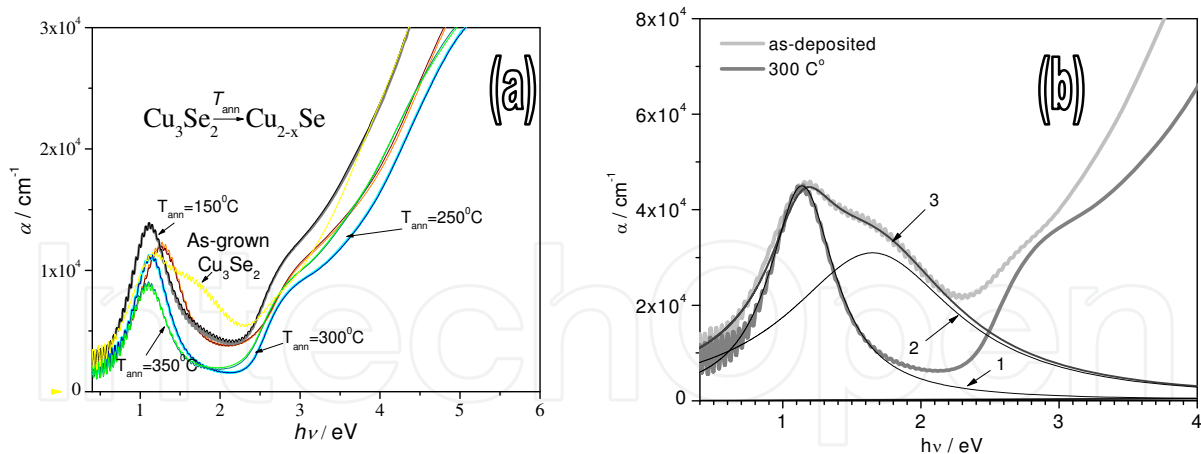


Fig. 18. (a) Variations of the absorption coefficient with photon energy ($h\nu$) for nanowired Cu_3Se_2 arrays in the alumina template pores before (1) and after (2-5) annealing for 90 min. The average diameter, spacing and height of species were 45 nm, 108 nm and approx. 0.5 μm , respectively. (b) Decompositional analysis of absorption spectra for as-deposited Cu_3Se_2 nanowired products. The calculated curves are Lorentzian's $[\sim(w/(4(h\nu-h\nu_0)^2+w^2))$, where $w \approx 0.58$ eV (FWHM), centered at 1.14 eV] for (1) and $[\sim(w/(4(h\nu-h\nu_0)^2+w^2))$, where $w \approx 1.48$ eV (FWHM), centered at 1.65 eV] (2), respectively. Curve (3) represents superposition of curves 1 and 2.

pulse duration of 2 ps, and the pulse repetition rate of 0.66 μJ). A Gaussian laser beam was focused with a 15 cm focal length lens to beam waist diameter of ~ 100 μm . A total power of the beam transmitted through the sample was measured in the field as a function of the sample position along the beam axis Z. This measurement corresponded to the standard open-aperture Z-scan procedure (Sheik-Banae et al. 1990). For the dynamic characterization of the optical nonlinearities, the laser beam was divided into two cross-polarized beams by a thin-film polarizer (Pačebutas et al. 2006). Using half-wave/polarizer pairs, beam intensities were changed independently; one of the beams was delayed in an optical delay line. The intensity of the probe beam was 30 times lower than that of the pump beam.

The results of a single-beam Z-scan measurement are presented in Figure 19. As seen from this Figure, the increase in intensity of the beam transmitted through copper selenide nanowires array at sample positions corresponding to the highest beam intensities can be evidenced for all the samples investigated. As the laser wavelength is within the defect absorption band of the samples, it could be assumed that this effect is caused by the bleaching of the defect-to-band transitions of the electrons. The density of defects participating in this transition can be estimated from the onset energy of the bleaching effect as $\sim 10^{20}$ cm^{-3} . The increase in the transmittance is especially pronounced for the specimens annealed at 150 and 200 $^\circ\text{C}$ (see curve 2). It correlates with the observed narrowing of the absorption peak in the range from 1 to 1.3 eV, and supports the idea of more homogeneous defect distribution obtained after annealing of the samples.

The dynamics of photoinduced transmission change in as-grown and annealed Cu_3Se_2 nanowire arrays studied by means of the pump-probe technique is presented in Figure 20. Relatively long photoexcited carrier lifetimes for all thermally treated specimens were obtained, indicating that this material system can be prospective for the manufacture of various optoelectronic devices, e.g. photovoltaic solar cells.

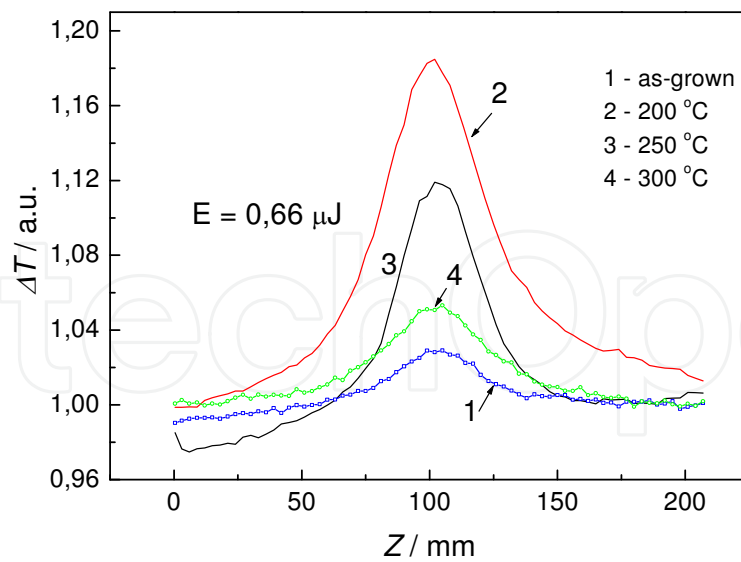


Fig. 19. Open-aperture Z-scan experimental data for Cu_3Se_2 nanowire arrays encased in alumina template by alternating current deposition before (1) and after (2-4) annealing at 200 (2), 250 (3) and 300 °C (4) for an hour. (pulse energy - 0.66 μJ , pulse duration - 2 ps).

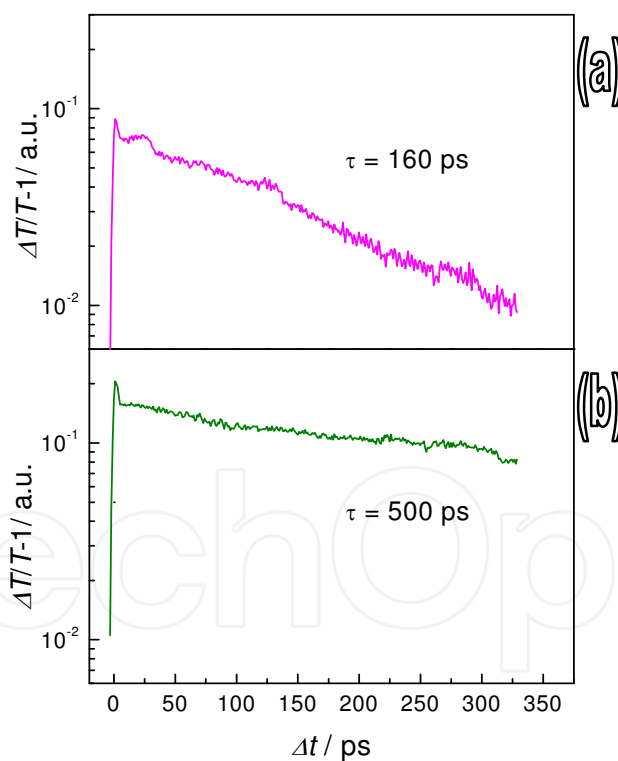


Fig. 20. Photoinduced transmission kinetics measured for Cu_3Se_2 nanowire arrays encased in alumina template by alternating current deposition in the solution as in Fig. 17 at 0.5 A dm^{-2} for 6 min after thermal treatment at 200 (a) and 250 °C (b). Pulse characteristics are the same as in Fig. 19.

A traditional femtosecond two-beam pump-probe spectroscopy technique was employed to study the kinetics of ultrafast non equilibrium charge carrier relaxation in copper selenide

nanowire arrays entrapped in alumina templates depending on the nanowires diameter, composition and excitation energy (Juška et al. 2009 a,b). The experimental results demonstrate that the transient absorption kinetics is almost independent of the excitation and probe wavelength and show a biexponential charge carrier recombination with the excitation intensity dependent decay rates. The initial ultrafast relaxation, which gets slower at higher excitation intensities, is followed by the slower decay component emerging at high intensities. These relaxation peculiarities were described by a theoretical model of two concurrent relaxation channels involving deep and shallow impurity levels (Fig. 21). Occupation of the valence band and shallow trapping levels leads to the absorption bleaching, which competes with the induced absorption due to transitions from these energy levels to higher energy states. The combined result of these competing optical effects is the bleaching of the impurity absorption band and the induced absorption at higher energies (Fig. 22).

We have found that the transient absorption properties are almost independent of the diameter of copper selenide nanowires within the range of 8 to 25 nm implying that low dimension effects such as spatial confinement and surface processes are of minor importance to relaxation processes. Recently we have also found that steady-state absorption spectra of copper selenide differing in the length of nanowires clearly differ. However, nonlinear optical effects in these arrays follow a very similar tendency, e.g.

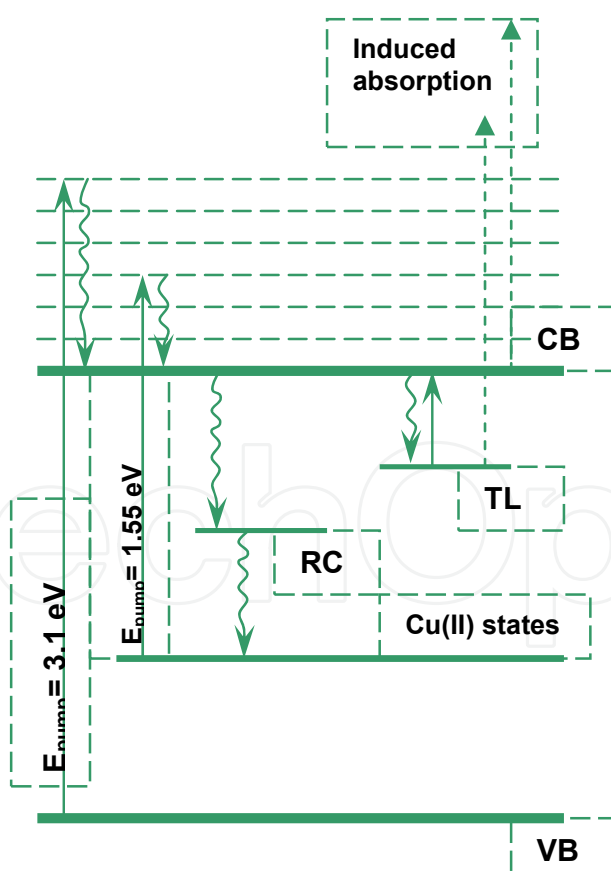


Fig. 21. Energetic diagram of Cu_{2-x}Se nanowires. Solid arrows indicate steady state absorption and excited state relaxation transitions. Dashed lines demonstrate induced absorption transitions.

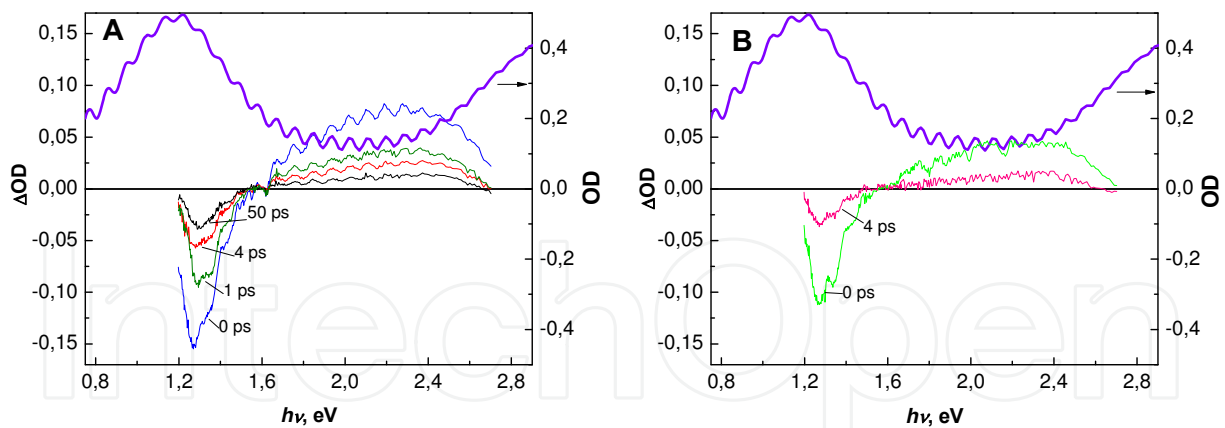


Fig. 22. Transient absorption spectra of the alumina matrix encased with Cu_{2-x}Se nanowire (\varnothing 13 nm) recorded at different delay times under 1.55 eV photon energy excitation with pulse intensity of 23 mJ/cm^2 (A) and under 3.1 eV excitation with pulse intensity of 13 mJ/cm^2 (B). Thick lines show the optical density of the sample. Spectra modulations are due to interference effects.

induced absorption dominates in the visible light spectra region while the bleaching band appears in IR. In contrast, the composition of copper selenide nanowires, changing upon annealing (see Fig. 18), is crucial for absorption peculiarities. In the case of nearly pure Cu_3Se_2 nanowire arrays, the initial relaxation is more expressed and leads to the formation of additional middle-gap states resulting in the rise of absorption bleaching in the visible light spectrum range. Furthermore, a higher concentration of defect states in Cu_3Se_2 and Cu_{2-x}Se mixture nanowires leads to an ultrafast and nearly complete recovery of temporal optical features.

The ability to adjust nonlinear optical features in copper selenide nanowires is very attractive for applications. As-formed and not annealed copper selenide nanostructures might be of a particular interest for nonlinear optical elements that require a fast optical response and a nearly complete recovery of bleaching. Annealed samples with a lower density of defects and local states can be used for devices that require longer lifetimes of nonequilibrium carriers.

5. Conclusion

A brief overview of the effect of heat treatments of some metallic (Fe, Sn) and semiconducting [$\text{FeO}(\text{OH})$, Cu_3Se_2 , Cu_{2-x}Se] nanowire arrays loaded inside the alumina template pores is presented herein for our recent research. Original results have been obtained for annealing of iron nanowire arrays eventually forming FeAl_2O_4 films. We suspect that annealing of some other metal nanowires, such as nickel and cobalt, encapsulated inside the alumina template pores and capable of forming spinel-type structures, can also result in the formation of MeAl_2O_4 films. These materials, demonstrating the new properties, are the focus of ongoing research in the field of spintronics. In contrast, the heating of nanowired metals, like tin, which can not form spinel-type materials results in the formation of metal oxide nanowire arrays. In this manner it is possible to fabricate nanowire arrays of novel barbed-shaped design due to diffusion of metal atoms into the

alumina cell walls robbing the oxygen from Al_2O_3 and destroying the matrix. These nanowires stand out for their extremely high surface area and core/shell morphology. Therefore, they can find interesting applications in catalysis.

With formation of new highly-ordered systems of nanowired arrays of Cu_2Se_3 and Cu_{2-x}Se in alumina matrices we are observing new non-linear optical behaviour of these semiconducting nanowire arrays that we are just beginning to interpret in terms of bleaching of the defect-to-band transitions of electrons in nanowires. Other semiconducting materials, such as iron oxyhydroxide, $\gamma\text{-FeO(OH)}$ (lepidocrocite) are being deposited inside the alumina pores and explored upon heating. It should be noted that by this way, we are able to form nanowired arrays of maghemite/hematite heterostructures, which have prospective applications in magnetic storage devices.

I hope that the idea of heat treatment of nanowired materials, encapsulated in alumina matrices, creates a simple and cheap route to manipulate their composition and properties, gaining novel prospective functionalities and applications. This approach, although still in very early stages of development, is expected to be of fundamental interest for future nanotechnologies.

Financial support of Lithuanian Science and Study Foundation through Research Project no. C07035 is acknowledged. I am very grateful for the indispensable help of my colleagues from Institute of Physics: Dalis Baltrūnas, Vidmantas Gulbinas, Kestutis Mažeika and Jonas Reklaitis; Arūnas Krotkus from Institute of Semiconductor Physics, Rolandas Tomašiūnas from Vilniaus University, Zenonas Jusys, Remigijus Juškėnas and Marytė Kurtinaitienė from Institute of Chemistry and Giulio Paolo Veronese from Istituto per la Microelettronica ed I Microsistemi del CNR, Bologna.

6. References

- D. AlMawlawi, N. Coombs & M. Moskovits. (1991). Magnetic properties of Fe deposited into anodic aluminium oxide pores as a function of particle size. *J. Appl. Phys.* Vol. 70(8), pp. 4421-4425, ISSN: 0021-8979
- J. D. Bernal, D. R. Dasgupta & A. L. Mackay. (1957). Oriented transformations in iron oxides and hydroxides. *Nature*, Vol. 180, pp. 645-647, ISSN: 0028-0836
- F. Blanc-Beguín, S. Nabily, J. Gieraltowski, A. Turzo, S. Querellou, P.Y. Salaun. (2009). Cytotoxicity and GMI bio-sensor detection of maghemite nanoparticles internalized into cells. *J. Mag. Mag. Mater.* Vol. 321(3) pp. 192-197, ISSN: 0304-8853
- P. M. Botta, R. C. Mercader, F. F. Aglietti & J. M. Porto Lopez. (2003). Synthesis of $\text{Fe-FeAl}_2\text{O}_4\text{-Al}_2\text{O}_3$ by high-energy ball milling of $\text{Al-Fe}_3\text{O}_4$ mixtures. *Scripta Materialia*, Vol. 48, pp. 1093-1098, ISSN: 1359-6462
- Q. Cai, J. Zhang, X. Chen, Z. Chen, W. Wang, G. Mo, Z. Wu, L. Zhang & W. Pan. (2008). Structural study on Ni nanowires in an anodic alumina membrane by using *in situ* heating extended x-ray absorption fine structure and x-ray diffraction techniques. *J. Phys.: Condens. Matter.*, Vol. 20, p. 115205, ISSN: 0953-8984
- K.-H. Choi, S.H. Lee, Y.-R. Kim, R. Malkinski, A. Vovk, Y. Barnakov, J.-H. Park, Y.-K. Jung & J.-S. Jung. (2007). Magnetic behaviour of Fe_3O_4 nanostructure fabricated by template method. *J. Mag. Mag. Mater.*, Vol. 310, pp. e861- e863, ISSN: 0304-8853

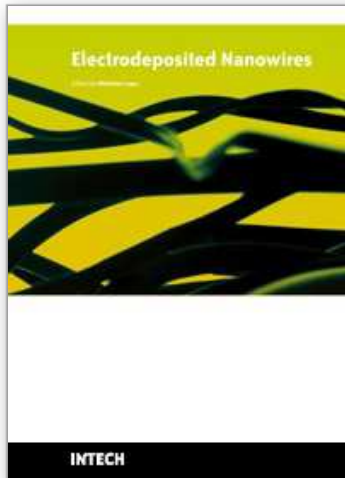
- A. N. Christensen, M. S. Lenmann & P. Convert. (1982). Deuteration of crystalline hydroxides. Hydrogen bonds of gamma $\text{AlOO}(\text{H,D})$ and gamma $\text{FeOO}(\text{H,D})$. *Acta Chem. Scand.*, Ser. A36, pp. 303-308, ISSN:0904-213X
- G. S. Collins, T. Kachnowski, N. Benczer-Koller & M. Pasternak. (1979). Application of the Mössbauer effect to the characterization of an amorphous tin-oxide system. *Phys. Rev. B*, Vol. 19(3), pp. 1369-1374, APS journal
- P. Colombari, S. Cherifi & G. Despert. (2008). Raman identification of corrosion products on automotive galvanized steel sheets, *J. Raman Spectrosc.*, Vol. 39 (7), pp. 881-886, Wiley InterScience, DOI:10.1002/jrs.1927
- R. M. Cornell & U. Schwertmann. (1996). *The Iron Oxides: Structure, Properties, Reactions, Occurrence and Uses*; VCH, Berlin
- X. Feng, J. Ma, F. Yang, F. Ji, F. Zong, C. Luan & H. Ma. (2008). Structural and photoluminescence properties of single crystalline SnO_2 : In films deposited on $\alpha\text{-Al}_2\text{O}_3$ (0001) by MOCVD. *J. Cryst. Growth*, Vol. 310(16), pp. 3718-3721, ISSN: 0022-0248
- S. Ferrere, A. Zaban & B.A. Gregg. (1997). Dye sensitization of nanocrystalline tin oxide by perylene derivatives. *J. Phys. Chem. B*. Vol. 101(23), pp. 4490-4493, ACS Publication, ISSN:1520-6106
- A. A. Firooz, A. R. Mahjoub & A. A. Khodadadi. (2008). Preparation of SnO_2 nanoparticles and nanorods by using a hydrothermal method at low temperature. *Mater. Lett.*, Vol. 62(12-13), pp. 1789-1792, ISSN: 0167-577X
- S. Fujihara, T. Maeda, H. Ohgi, E. Hosono, H. Imai & S.-H. Kim. (2004). Hydrothermal routes to prepare nanocrystalline mesoporous SnO_2 having high thermal stability. *Langmuir*, Vol. 20, pp. 6476- 6481, ISSN:0743-7463
- C. X. Gao, Q. F. Liu & D. S. Xue. (2002). Fabrication and characterization of amorphous $\beta\text{-FeOOH}$ nanowire arrays. *J. Mater. Sci. Lett.*, Vol. 21, No. 22, pp. 1781-1783, ISSN: 0261-8028
- A. U. Gehring & A. M. Hofmeister. (1994). The transformation of lepidocrocite during heating; a magnetic and spectroscopic study. *Clays Clay Miner.* Vol. 42, pp. 409-415, ISSN: 1552-8367
- H. Gleiter. (2000). Nanostructured materials: basic concepts and microstructure. *Acta Mater.*, Vol. 48, pp. 1-29, ISSN:1359-6454
- F. Gu, S.F. Wang, C.F. Song, M.K. Lü, Y.X. Qi, G.J. Zhou, D. Xu & D.R. Yuan. (2003). Synthesis and luminescence properties of SnO_2 nanoparticles. *Chem. Phys. Lett.*, Vol. 372(3-4), pp. 451-454, ISSN:0009-2614
- A. M. Hermann & L. Fabick. (1983). Research on polycrystalline thin-film photovoltaic devices. *J. Cryst. Growth*, Vol. 61(3), pp. 658-664, ISSN:0022-0248
- A. Jagminas, D. Bigelienė, I. Mikulskas, R. Tomašiūnas. (2001). Growth peculiarities of aluminium oxide at high voltages in diluted phosphoric acid. *J. Cryst. Growth*, Vol. 233, pp. 591-598, Elsevier, ISSN:0022-0248
- A. Jagminas, R. Juškėnas, I. Gailiūtė, G. Statkutė & R. Tomašiūnas. (2006). Electrochemical synthesis and optical characterization of copper selenide nanowire arrays within the alumina pores. *J. Cryst. Growth*, Vol. 294(2), pp. 343-348, ISSN: 0022-0248

- A. Jagminas, K. Mažeika J. Reklaitis, M. Kurtinaitienė & D. Baltrūnas. (2008). Template synthesis, characterization and transformations of iron nanowires while aging. *Mat. Chem. Phys.* Vol. 109, pp. 82-86, ISSN: 0254-0584
- A. Jagminas, K. Mažeika J. Reklaitis, V. Pakštas & D. Baltrūnas. (2009a). Annealing effects on the transformations of Fe nanowires encapsulated in the alumina template pores. *Mat. Chem. Phys.*, Vol. 115, pp. 217-222, ISSN: 0254-0584
- A. Jagminas, K. Mažeika, E. Juška, J. Reklaitis, D. Baltrūnas, R. Schmidt. M(2009b). Fabrication and characterization of lepidocrocite (γ -FeOOH) nanowire arrays. *Appl. Surf. Sci.* (subm.)
- A. Jagminas, R. Tomašiūnas, A. Krotkus, R. Juškėnas & G. Aleksejenko. (2009c). Fabrication and phase variation in annealed Cu_3Se_2 nanowire arrays. *Appl. Surf. Sci.*, Vol. 255(17), pp. 7739-7742, Elsevier, ISSN:0169-4332
- O. Jessensky, F. Müller & U. Gösele. (1998). Self-organized formation of hexagonal pore arrays in anodic alumina. *Appl. Phys. Lett.*, Vol. 72, pp. 1173-1175, ISSN: 0003-6951
- Z. Ji, Z. He, Y. Song, K. Liu & Y. Xiang. (2004). *Thin Solid Films*, Vol. 460, pp. 324-326, ISSN: 0040-6090
- G. Juška, A. Jagminas & V. Gulbinas. (2009a). Excitation relaxation in copper selenide nanowires. *Phys. Status Solidi B*, Vol 246 (5), pp. 1082-1087, Wiley Inter Sci., ISSN:
- G. Juška, V. Gulbinas & A. Jagminas. (2009b). Transient absorption of copper selenide nanowires of different stoichiometric structure. *Lithuan. J. of Phys.* (subm.)
- M. Kokonou, K.P. Giannakopoulos & A. G. Nassiopoulou. (2007). Few nanometer thick anodic porous alumina films on silicon with high density of vertical pores. *Thin Solid Films*, Vol. 515, pp. 3602-3606, Elsevier, ISSN:0040-6090
- X. Kong, D. Yu & Y. Li. (2003). Synthesis of SnO_2 nanoribbons by direct oxidation of tin powders. *Chem. Lett.*, Vol. 32, pp. 100-101, The Chemical Soc. of Japan, ISSN:0366-7022
- E. Kuzmann, S. Nagy and A. Vertes. (2003). Critical review of analytical applications of Mössbauer spectroscopy illustrated by mineralogical and geological examples. *Pure Appl. Chem.*, Vol. 75(6), pp. 801-858, IUPAC publications, ISSN:0033-4545
- L. Li, Y. Zhang, Y. W. Yang, X. H. Huang, G. H. Li & L. D. Zhang. (2005). Diameter-dependent thermal expansion properties of Bi nanowire arrays. *Appl. Phys. Lett.*, Vol. 87, p. 031912, ISSN: 0003-6951
- H. Masuda & K. Fukuda. (1995). Ordered metal nanohole arrays made by a two-step replication of honeycomb structures of anodic alumina. *Science*, Vol. 268, pp. 1466-1468, ISSN:1466-1468
- R. M. Metzger, V. V. Konovalov, M. S. T. Xu, G. Zangari, B. Xu, M. Benakli & W. D. Doyle. (2000). Magnetic nanowires in hexagonally ordered pores of alumina. *IEEE Trans. Magn.*, Vol. 36(1), pp. 30-35, ISSN:0018-9464
- M. P. Morales, M. J. Muñoz-Aguado, J. L. Garcia-Palacios, F. J. Lazaro & C. J. Serna. (1998). Coercitivity enhancement in $\gamma\text{-Fe}_2\text{O}_3$ particles dispersed at low volume fraction. *J. Magn. Magn. Mater.*, Vol.183, pp. 232-240, ISSN:0304-8853

- Ö. Özdemir & D. J. Dunlop. (1993). Chemical remanent magnetization during gamma-FeOOH phase transformations. *J. Geophys. Res.* Vol. 98, No B3, pp. 4191-4198, ISSN:0148-0227
- V. Pačebutas, G. Aleksejenko, A. Krotkus, J. W. Ager, W. Walukiewicz, H. Liu & W. J. Schaff. (2006). Optical bleaching effect in InN epitaxial layers. *Appl. Phys. Lett.*, Vol. 88, p. 191109, ISSN:0003-6951
- X. Peng, G. Wu, P. Holt-Hindle & A. Chen. (2008). Growth and characterization of free-standing single crystalline tin and tin oxide nanobelts. *Mater. Lett.*, Vol. 62, pp. 1969-1972, ISSN:0167-577X
- R. E. Presley, C. L. Munsee, C.-H. Park, H. Hong, J. F. Wager & D.A. Keszler. (2004). Tin oxide transparent thin-film transistors. *J. Phys. D: Appl. Phys.*, Vol. 37(20), pp. 2810-2813, Institute of Physics Publishing, ISSN:0022-3727
- D. Qin, P. Yan, G. Li, J. Xing & Y. An. (2008). Self-construction of SnO₂ cubes based on aggration of nanorods. *Mater. Lett.*, Vol. 62(16), pp. 2411-2414, ISSN:0167-577X
- J. Qin, J. Nogues, M. Mikhaylova, A. Roig, J. S. Munoz & M. Muhammed. (2005). Differences in the magnetic properties of Co, Fe, and Ni 250-300 nm wide nanowires electrodeposited in amorphous anodized alumina templates. *Chem. Mater.* Vol. 17(7), pp. 1829-1834, ACS Journal, ISSN:1520-5002
- W. Römer & C. Steinem. (2004). Impedance Analysis and Single-Channel Recordings on Nano-Black Lipid Membranes Based on Porous Alumina. *Biophysical Journal*, Vol. 86, pp. 955-965, ISSN:0006-3495
- D. Schroerer & R. C. Nininger. (1967). Morin transition in α -Fe₂O₃ microcrystals. *Phys. Rev. Lett.*, Vol. 19, pp. 632-654, ISSN:1079-7114
- M. Sheik-Bahae, A. A. Said, T. H. Wei, D. J. Hagan & E. W. Van Stryland. (1990). Sensitive measurement of optical nonlinearities using a single beam. *IEEE J. Quantum Electron*, Vol. 26(4), pp. 760-769, ISSN: 0018-9197
- J.-O. Song & T.-Y. Seong (2004). Highly transparent Ag/SnO₂ ohmic contact to *p*-type GaN for ultraviolet light-emitting diodes. *Appl. Phys. Lett.*, Vol. 85, p. 6374, American Institute of Physics, DOI:10.1063/1.1834990
- G. Statkutė, A. Jagminas & R. Tomašiūnas. (2008). Photo-induced transmittance in copper-selenide nanowires. *Opt. Mater.*, Vol. 30, pp. 743-745, Elsevier, ISSN:0925-3467
- J. Sundqvist, J. Lu, M. Ottosson & A. Harsta. (2006). Growth of SnO₂ thin films by atomic layer deposition and chemical vapour deposition: A comparative study. *Thin Solid Films*, Vol. 514, pp. 63-68, ISSN: 0040-6090
- G. E. Thompson. (1997). Porous anodic alumina: fabrication, characterization and applications. *Thin Solid Films*, Vol. 297, pp. 192-201, ISSN:0040-6090
- Y. Wang, J. Yang, C. Ye, X. Fang & L. Zhang. (2004). Thermal expansion of Cu nanowire arrays. *Nanotechnology*, Vol. 15, pp. 1437-1440, ISSN:0957-4484
- Y. Wang, J. Y. Lee & H. C. Zeng. (2005). Polycrystalline SnO₂ nanotubes prepared via infiltration casting of nanocrystallites and their electrochemical application. *Chem. Mater.*, Vol. 17(15), pp. 3899-3903, ACS Publications, DOI:10.1021/cm050724f
- X. J. Xu, G. T. Fei, W. H. Yu, L. Chen & L. D. Zhang. (2006). *In situ* x-ray diffraction study of the thermal expansion of the ordered arrays of silver nanowires embedded

- in anodic alumina membranes. *Appl. Phys. Lett.*, Vol. 88, p. 211902, ISSN: 0003-6951
- X. Xu, Z. Wang, T. Zhang, X. Zeng, W. Xu, J. Zhang, J. Yan, J. Zhang, L. Zhang. (2008). Manipulation of optical properties of Ag/Cu alloy nanowire arrays embedded in anodic alumina membranes. *Appl. Surf. Sci.*, Vol. 254, pp. 3845-3848, ISSN:0169-5332
- Li-Y. Zhang, J. Fen & De-S. Hue. (2007). An investigation of thermal decomposition of β -FeOOH nanowire arrays assembled in AAO templates. *Mater. Lett.*, Vol. 61(6), pp. 1363-1367 ISSN:0167-577X

IntechOpen



Electrodeposited Nanowires and their Applications

Edited by Nicoleta Lupu

ISBN 978-953-7619-88-6

Hard cover, 228 pages

Publisher InTech

Published online 01, February, 2010

Published in print edition February, 2010

The book offers a new and complex perspective on the fabrication and use of electrodeposited nanowires for the design of efficient and competitive applications. While not pretending to be comprehensive, the book is addressing not only to researchers specialized in this field, but also to Ph.D. students, postdocs and experienced technical professionals.

How to reference

In order to correctly reference this scholarly work, feel free to copy and paste the following:

Arūnas Jagminas (2010). Annealing Effects on the Metal and Semiconductor Nanowires Loaded Inside the Alumina Pores, *Electrodeposited Nanowires and their Applications*, Nicoleta Lupu (Ed.), ISBN: 978-953-7619-88-6, InTech, Available from: <http://www.intechopen.com/books/electrodeposited-nanowires-and-their-applications/annealing-effects-on-the-metal-and-semiconductor-nanowires-loaded-inside-the-alumina-pores>

INTECH
open science | open minds

InTech Europe

University Campus STeP Ri
Slavka Krautzeka 83/A
51000 Rijeka, Croatia
Phone: +385 (51) 770 447
Fax: +385 (51) 686 166
www.intechopen.com

InTech China

Unit 405, Office Block, Hotel Equatorial Shanghai
No.65, Yan An Road (West), Shanghai, 200040, China
中国上海市延安西路65号上海国际贵都大饭店办公楼405单元
Phone: +86-21-62489820
Fax: +86-21-62489821

© 2010 The Author(s). Licensee IntechOpen. This chapter is distributed under the terms of the [Creative Commons Attribution-NonCommercial-ShareAlike-3.0 License](#), which permits use, distribution and reproduction for non-commercial purposes, provided the original is properly cited and derivative works building on this content are distributed under the same license.

IntechOpen

IntechOpen